Remote Sensing of Environment 264 (2021) 112581

Contents lists available at ScienceDirect

Remote Sensing of Environment

journal homepage: www.elsevier.com/locate/rse

Mapping and classification of volcanic deposits using multi-sensor unoccupied aerial systems

Brett B. Carr [a,b,*], Einat Lev [a], Theresa Sawi [a], Kristen A. Bennett [c], Christopher S. Edwards [d], S. Adam Soule [e], Silvia Vallejo Vargas [f], Gayatri Indah Marliyani [g]

[a] Lamont-Doherty Earth Observatory, Columbia University, 61 Route 9W, Palisades, NY 10964, USA
[b] U.S. Geological Survey, Hawaiian Volcano Observatory, 1266 Kamehameha Ave., Suite A8, Hilo, HI 96720, USA
[c] U.S. Geological Survey, Astrogeology Science Center, 2255 N. Gemini Dr., Flagstaff, AZ 86001, USA
[d] Department of Astronomy and Planetary Science, Northern Arizona University, PO Box 6010, Flagstaff, AZ 86011, USA
[e] Woods Hole Oceanographic Institution, 266 Woods Hole Road, MS #24, Woods Hole, MA 02543, USA
[f] Instituto Geofísico, Escuela Politécnica Nacional, Ladrón de Guevara E11-253, Quito 170525, Ecuador
[g] Department of Geological Engineering, Faculty of Engineering, Universitas Gadjah Mada, FT UGM Jl. Grafika No. 02, Yogyakarta 55281, Indonesia

ARTICLE INFO

Edited by: Jing M. Chen

Keywords:
Thermal remote sensing
Unoccupied aerial systems (UAS)
Lava flows
Land surface classification
Mapping of volcanic deposits

ABSTRACT

The deposits from volcanic eruptions represent the record of activity at a volcano. Identification, classification, and interpretation of these deposits are crucial to the understanding of volcanic processes and assessing hazards. However, deposits often cover large areas and can be difficult or dangerous to access, making field mapping hazardous and time-consuming. Remote sensing techniques are often used to map and identify the deposits of volcanic eruptions, though these techniques present their own trade-offs in terms of image resolution, wavelength, and observation frequency. Here, we present a new approach for mapping and classifying volcanic deposits using a multi-sensor unoccupied aerial system (UAS) and demonstrate its application on lava and tephra deposits associated with the 2018 eruption of Sierra Negra volcano (Galápagos Archipelago, Ecuador). We surveyed the study area and collected visible and thermal infrared (TIR) images. We used structure-from-motion photogrammetry to create a digital elevation model (DEM) from the visual images and calculated the solar heating rate of the surface from temperature maps based on the TIR images. We find that the solar heating rate is highest for tephra deposits and lowest for ʻaʻā lava, with pāhoehoe lava having intermediate values. This is consistent with the solar heating rate correlating to the density and particle size of the surface. The solar heating rate for the lava flow also decreases with increasing distance from the vent, consistent with an increase in density as the lava degasses. We combined the surface roughness (calculated from the DEM) and the solar heating rate of the surface to remotely classify tephra deposits and different lava morphologies. We applied both supervised and unsupervised machine learning algorithms. A supervised classification method can replicate the manual classification while the unsupervised method can identify major surface units with no ground truth information. These methods allow for remote mapping and classification at high spatial resolution (< 1 m) of a variety of volcanic deposits, with potential for application to deposits from other processes (e.g., fluvial, glacial) and deposits on other planetary bodies.

1. Introduction

Characterization of the morphology and physical characteristics (e.g., grain size, density) of volcanic deposits such as lava flows, tephra, and pyroclastic density currents (PDCs) is fundamental to the ability to understand the eruption and emplacement processes that produced the deposits. Insight on eruption processes gained from the study of their deposits is key to interpreting the history and eruptive potential of volcanic areas, especially in cases where eruptions were not directly observed. Detailed knowledge of the volcanic history of a region

* Corresponding author at: Lamont-Doherty Earth Observatory, Columbia University, 61 Route 9W, Palisades, NY 10964, USA.
E-mail addresses: bcarr@usgs.gov (B.B. Carr), einatlev@ldeo.columbia.edu (E. Lev), tsawi@ldeo.columbia.edu (T. Sawi), kbennett@usgs.gov (K.A. Bennett), Christopher.Edwards@nau.edu (C.S. Edwards), ssoule@whoi.edu (S.A. Soule), svallejo@igepn.edu.ec (S. Vallejo Vargas), gayatri.marliyani@ugm.ac.id (G.I. Marliyani).

https://doi.org/10.1016/j.rse.2021.112581
Received 10 June 2021; Accepted 1 July 2021
Available online 4 August 2021
0034-4257/Published by Elsevier Inc.

facilitates progress towards many objectives, from hazard assessment and mitigation for future eruptions to investigations of the evolution of planetary surfaces.

Lava flow morphology can be used to infer lava properties (e.g., viscosity, temperature) and emplacement dynamics (Fink and Griffiths, 1992; Griffiths, 2000). As an example, for a similar lava viscosity, ʻaʻā morphology is indicative of a higher flow rate relative to pāhoehoe morphology. For similar flow rate, ʻaʻā indicates higher viscosity (Lipman and Banks, 1987; Whelley et al., 2017). Different lava flow morphologies are characterized by different surface roughness. At length scales of 1–10 m, pāhoehoe lava generally has smoother texture than ʻaʻā (Lipman and Banks, 1987; Whelley et al., 2017). Lava flows are in general rougher than tephra deposits, which consist of smaller clasts of ash and scoria. Depositional distinctions also exist among PDC deposits. Debris avalanches, pyroclastic flows, and pyroclastic surges have characteristic grain size distributions, morphology, or roughness relative to each other (Charbonnier and Gertisser, 2008; Whelley et al., 2014; Solikhin et al., 2015).

Unfortunately, volcanic deposits can be difficult and dangerous to access and navigate on foot. In addition, deposit areas are often too extensive or remote to be mapped effectively with limited time or personnel. The ability to remotely describe and quantify volcanic deposits is thus highly valuable and numerous remote sensing techniques utilizing ground-based, airborne, and satellite instruments have been developed to observe a variety of volcanic processes and deposits (e.g., Wooster et al., 2000; Whelley et al., 2014; Solikhin et al., 2015; Ganci et al., 2018; Pallister et al., 2019; Corradino et al., 2019). The rise of unoccupied aerial systems (UAS) technology in recent years as a cost-effective and efficient means to conduct airborne surveys has further facilitated several advancements in volcanological mapping (James et al., 2020a, and references therein).

We describe a new approach in which we classify and map lava flow morphology and tephra deposits from a volcanic eruption by combining data derived from UAS-mounted visual and thermal infrared (TIR) cameras. From the collected images, we produced two separate remotely sensed data sets describing the study area's surface roughness and its solar heating rate (a proxy for its thermal inertia). Such data sets are often used to characterize surface types, albeit separately. They are sensitive to different properties of the surface, and thus their combination allows for more accurate and consistent identification of surface types than either quantity alone. Based on the mapped locations of the surface types we classify; we can make interpretations about the mechanisms of flow emplacement during the eruption. Additionally, roughness and thermal inertia proxies are commonly calculated from satellite data, and our technique deriving these values from UAS surveys provides comparable datasets with an increase in spatial resolution of more than an order of magnitude in most cases. This method has applications for using UAS to better understand the history of eruptive processes in volcanic areas by facilitating multi-scale investigations of volcanic deposits and improving the safety and efficiency of field mapping.

1.1. Surface roughness of volcanic deposits

The surface roughness of volcanic deposits can be used to identify different morphological units using remotely sensed data. Roughness is typically calculated from a digital elevation model (DEM) that can be produced using radar (Morris et al., 2008; Richardson and Karlstrom, 2019), light detection and ranging (LiDAR) (Mazzarini et al., 2009; Whelley et al., 2014; Whelley et al., 2017), or photogrammetric (Bretar et al., 2013) data sources that can be satellite-, airborne-, or ground-based. However, there is no standard unit or method for calculating roughness. Grohmann et al. (2011) evaluated several methods, including: surface area to plan area ratio, surface normal vector dispersion, the standard deviation of elevation, the standard deviation of residual topography after subtracting a smoothed DEM, the standard deviation of slope, and the standard deviation of profile curvature. These methods all invoke a "neighborhood" (i.e., a moving window of a given size), where the roughness is determined by comparing the pixel values within a region centered on the pixel for which the roughness value will be assigned. The size of the region/moving window is determined by the user for reasons that can include the DEM resolution and the scale of interest (e.g., smaller window size is more sensitive to relatively minor topographic changes whereas a larger window size will better generalize the terrain) (Shepard et al., 2001). Of the methods evaluated, Grohmann et al. (2011) found the standard deviation of slope to be the preferred method for geomorphology, citing the simplicity of the calculation, detection of both fine and regional scale relief, and consistent performance regardless of DEM or moving window scale.

For applications of surface roughness focused only on local (as opposed to regional) roughness features, a common technique is to first detrend the DEM to remove background or regional slopes (Shepard et al., 2001; Whelley et al., 2014; Whelley et al., 2017; Richardson and Karlstrom, 2019). Roughness can then be calculated by various methods, including the standard deviation or root-mean-square of the residual elevations (Whelley et al., 2014), or the application of a 2D discrete Fourier transform (Richardson and Karlstrom, 2019).

Roughness derived from LiDAR surveys has been used to classify and map volcanic deposits including both pyroclastic deposits (Mazzarini et al., 2009; Whelley et al., 2014) and lava flows (Morris et al., 2008; Whelley et al., 2017). These studies applied statistical analyses either directly to the elevation data (Morris et al., 2008; Mazzarini et al., 2009) or to roughness values derived from residual elevations after detrending the DEM (Whelley et al., 2014, 2017). The statistical measures allowed for multi-component analyses that showed grain size and deposit thickness control roughness in pyroclastic deposits (Mazzarini et al., 2009) and identified how measurements of roughness varied depending on both lava flow morphology and the spatial resolution at which the roughness was calculated. Whelley et al. (2014, 2017) found that the mean roughness value, homogeneity, and entropy calculated for a neighborhood around each pixel to be best at distinguishing different surface types. Using this technique, distinct mappable units in the Mt. St. Helens pumice plain (e.g., channels, pumice lobes, debris avalanches; Whelley et al., 2014) and the 1974 Mauna Ulu lava flow (e.g., ʻaʻā, pāhoehoe, slabby pāhoehoe, overflow ʻaʻā; Whelley et al., 2017) were identified by visually grouping areas sharing similar roughness texture statistics.

1.2. Thermophysical properties of volcanic deposits

Different surface types or morphologies also vary in their thermophysical properties, such as thermal inertia, and can be identified using TIR remote sensing (Ramsey and Fink, 1999; Price et al., 2016; Ramsey et al., 2016; Simurda et al., 2020). Thermal inertia is a physical material property that is related to the resistance to temperature change and is commonly derived by modeling observations of the diurnal temperature response of a surface (Ramsey et al., 2016; Simurda et al., 2020). Thermal inertia (*TI*) is defined as:

$$TI = \sqrt{k\rho c} \quad (1)$$

where k is thermal conductivity (J s^{-1} m^{-1} K^{-1}), ρ is density (kg m^{-3}), and c is the specific heat (J K^{-1} kg^{-1}), such that the units of thermal inertia are J m^{-2} K^{-1} $s^{-1/2}$. In general, lower thermal inertia (low resistance to temperature change) is associated with finer–grained and/or unconsolidated material (such as dust or sand) while higher thermal inertia (high resistance to temperature change) corresponds to larger particle sizes and/or densely packed grains (i.e., bedrock) (Ramsey et al., 2016; Fergason et al., 2006; Price et al., 2016; Simurda et al., 2020). Thermal inertia is sensitive to grain size because the number of grain-to-grain contacts decreases with increasing particle size (as the solid phases have significantly higher thermal conductivity than the

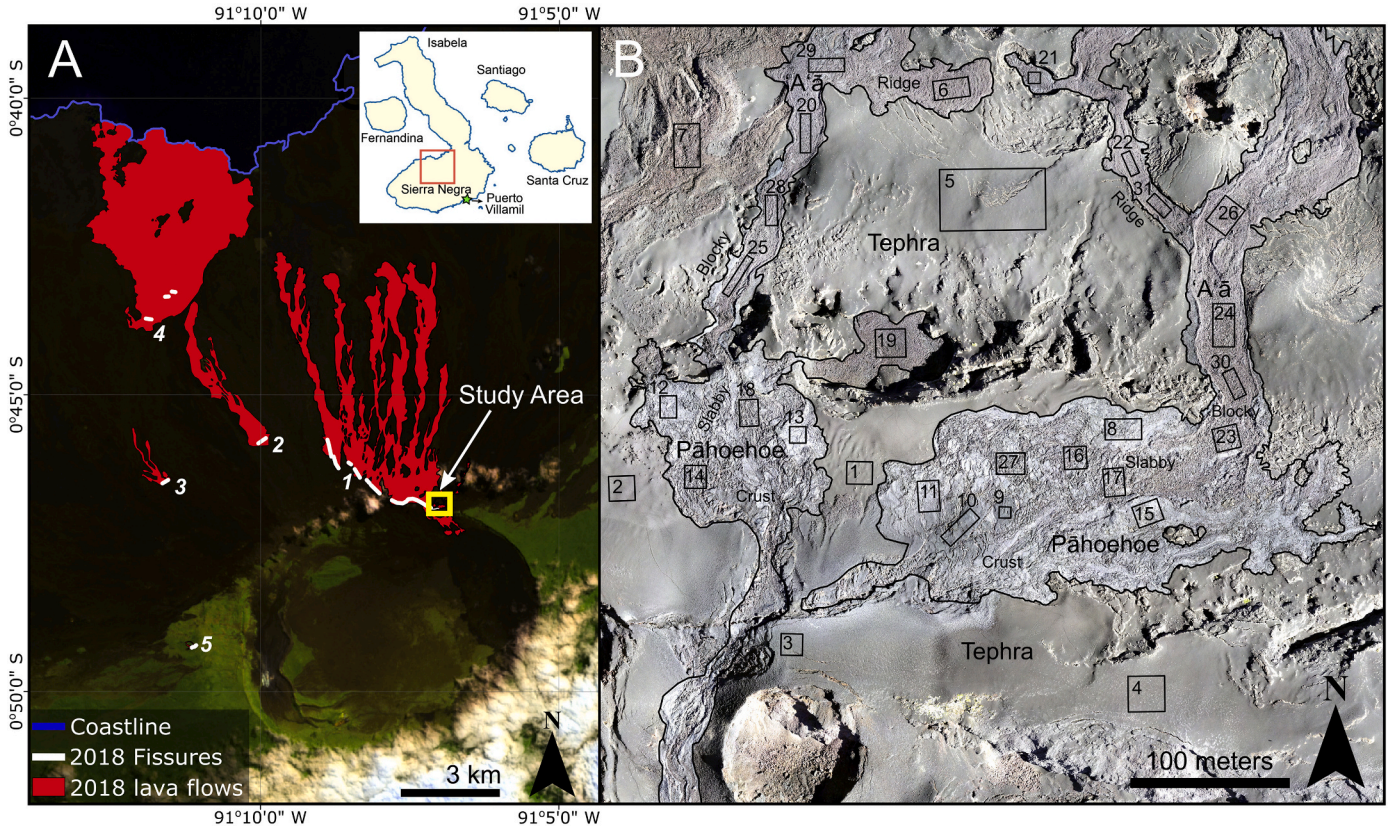

Fig. 1. Location of Sierra Negra volcano. The 2018 eruption of Sierra Negra occurred along a series of fissures on the north caldera rim and north flank (A, modified from Vasconez et al., 2018). Numbered white lines mark the fissure locations and the red areas are the lava flows. Inset in (A) shows Sierra Negra's location (red box) on Isla Isabela in the Galápagos Archipelago. The study area (yellow box, A) is located near the caldera rim and includes vents from fissure 1. The orthophoto of the study area (B) was created with visual images from Flight 2 of the UAS survey and has a spatial resolution of 0.04 m. The 2018 lava flows are outlined in black. Numbered boxes are the regions used to define the manual classification. Labels indicate surface types that were visually identified during field work and from inspection of the UAS images. Satellite basemap in (A) courtesy of https://earthexplorer.usgs.gov/. (For interpretation of the references to colour in this figure legend, the reader is referred to the web version of this article.)

pore-filling gasses). Thus, larger particles can more efficiently conduct heat into the sub-surface as compared to smaller particles, where the numerous grain-to-grain contacts restrict the thermal conductivity. Over a diurnal cycle of solar heating, lower thermal inertia materials/surfaces will heat (and cool) faster compared to high thermal inertia materials/surfaces, ultimately reaching higher daytime temperatures and lower nighttime temperatures.

As the material properties used by Eq. 1 are not possible to measure remotely, an apparent thermal inertia (ATI) has been defined as

$$ATI = (1 - a)/(\Delta T) \quad (2)$$

where a is the albedo of the land surface over the visible/near-infrared and short-wave infrared wavelengths and ΔT is the difference in brightness temperature between day and night TIR images (Price, 1977). ATI is inversely proportional to the temperature difference in two thermal images acquired over the diurnal cycle (Simurda et al., 2020). Measurements of ATI or, more generally, the heating rate between observations of a shorter duration, have been used as a proxy for thermal inertia, and utilize data from TIR sensors on satellites (Price, 1977; Scheidt et al., 2010; Price et al., 2016; Simurda et al., 2020) or, in our case, a UAS.

Thermal inertia is commonly used to investigate planetary surfaces, notably Mars, where the value can provide information on the degree of mantling by dust and the presence of exposed bedrock (Ramsey et al., 2016; Fergason et al., 2006). Crown and Ramsey (2017) found highly variable thermal signals on small spatial scales for lava flows in Arsia Mons, indicating complex relations between the rough and blocky surface of lava flows and mantling by fine-grained material. For terrestrial targets, the Earth's thick and highly variable atmosphere and vegetation complicate estimates of thermal inertia from satellite (Price, 1977; Simurda et al., 2020). However, satellite-derived ATI has been used to investigate, for example, soil moisture (Price, 1977; Scheidt et al., 2010) and tephra mantling of lava flows (Price et al., 2016; Simurda et al., 2020). Simurda et al. (2020) have recently demonstrated that relating grain size to heating rate or ATI observed from orbit is influenced by sub-pixel roughness, where surfaces with different roughness characteristics (and thus, different ATI) can be present within a single pixel (90 m spatial resolution in Simurda et al., 2020). They found that the highest ATI values were associated not with surfaces with predominantly coarse-size grains as would be expected, but rather with surfaces containing moderate-sized grains. The ATI of surfaces with coarse grain sizes, they discovered, was lowered due to self-shadowing and the trapping of fines by the coarse grains. In our study investigating relative thermal inertia we utilize both a multi-sensor approach and a high spatial resolution visible dataset, as recommended in Simurda et al. (2020). Data from TIR sensors are also sensitive to density (e.g., Eq. 1). Ramsey and Fink (1999) demonstrated this concept for volcanic deposits, using multi-band airborne TIR imagery to quantify the vesicularity of silicic lava flows.

1.3. Sierra Negra volcano, Ecuador

Sierra Negra volcano (1124 m a.s.l.) is one of six large basaltic shield volcanoes that form Isla Isabela in the Galápagos Archipelago of Ecuador

Table 1
UAS flight and SfM photogrammetry data. Three UAS flights were conducted at Sierra Negra on October 22, 2018 to capture the visual and TIR images used to generate the SfM photogrammetry-derived temperature maps (Fig. 2, used to calculate solar heating rate), orthophoto (Fig. 1b), and DEM (used to calculate surface roughness).

Flight	Time[a]	Flight Duration (minutes)	Image Type	Photos in Model	Dense Cloud Points	Orthophoto Resolution (m)	DEM Resolution (m)	Alignment Error[b] (m)	T_{min} (°C)[c]	T_{max} (°C)[c]
1	07:15	24	TIR	474	4,861,830	0.17		0.19	7.9	134.6
2	08:30	24	TIR	490	5,153,991	0.19		0.18	10.7	124.2
			Visual	487	161,460,941	0.04	0.08	NA		
3	09:45	22	TIR	443	4,895,841	0.18		0.13	13.7	134.9

[a] UAS in flight at this time. Takeoff times were: 7:11 am, 8:18 am, and 9:35 am. Times are local (GMT-06).
[b] Control point alignment error of TIR orthophoto to Flight 2 visual orthophoto (17 control points used).
[c] Maximum and minimum temperatures for any single pixel in any single image from the specified flight- used for the linear scaling (Eq. 3).

(Fig. 1). The volcano is characterized by a large (7 × 10.5 km) summit caldera. Sierra Negra erupts frequently, with events in 2018, 2005, and 1979 (Geist et al., 2007; Vasconez et al., 2018). Activity during recent eruptions has been focused along fissures on the northern crater rim and on the north flank, which fed lava flows that traveled both down the north flank and into the caldera (Geist et al., 2007; Vasconez et al., 2018). The 2018 eruption of Sierra Negra began on June 26. A series of fissures (Fig. 1a) opened along and to the north of the north rim of the summit caldera (Vasconez et al., 2018). Lava flows descended as far as 7 km down the north slope of the volcano, and one flow went into the caldera. This phase of the eruption with multiple active fissures lasted less than 24 h and the emplacement of lava flows was complete within 1–2 days (Vasconez et al., 2018). Following the 26 June activity, the eruption moved downslope to the northwest. Sustained effusion from fissure 4 (Fig. 1a) fed a large lava flow field that entered the ocean (Vasconez et al., 2018). The eruption ended on 23 August 2018.

We visited the eruption site in October 2018, roughly four months after the summit eruption ended. The lava flows observed for this study (Fig. 1b) were emplaced on terrain consisting of lava flows, tephra, craters, and fissures from previous eruptions. Pāhoehoe morphology dominated in proximity to the vents but transitioned quickly (within a few hundred meters or less) to ʻaʻā for most of the flow length. Our study area (Fig. 1b) is a roughly 0.5 km^2 region that includes two vents from fissure 1 (to the immediate west and northeast of Region 3, Fig. 1b). Each vent fed a lava flow that traveled downslope to the north. Multiple flow branches and lobes break off from the main channels, and in one place the lava has filled the floor of a crater (Region 19, Fig. 1b). Flow thickness is generally no more than a few meters (Vasconez et al., 2018).

2. Methods

2.1. UAS surveys

We used a DJI Matrice 210 (M210) quadcopter for this study. The M210 has two gimbal-stabilized camera mounts, on which a DJI Zenmuse X4S visual camera and a DJI Zenmuse XT TIR camera were mounted. The Zenmuse X4S has a 20-megapixel (MP), 1" CMOS (complementary metal oxide semiconductor) sensor with a mechanical shutter and an 8.8 mm focal length. The Zenmuse XT is a FLIR Tau 640 with an uncooled VOx Microbolometer, focal plane array of 640 × 512 pixels (0.3 MP), and a 30 hertz frame rate. The sensor is sensitive to a 7.5–13.5 μm spectral band, has a sensitivity of < 50 mK, and accuracy of ±5 °C. The Zenmuse XT is sensitive to a temperature range of -25–135 °C in the high-gain setting and to a range of -25–550 °C in the low-gain setting. As deposits surveyed in this study were cooled from their original emplacement, we used the high-gain setting. Equipped with these cameras, the M210 has a maximum flight time of approximately 25 min.

The location of the survey region within the extent of recent eruptive deposits (Fig. 1) was chosen such that multiple types of volcanic deposits (e.g., tephra and different lava flow morphologies) would be present in the resulting data products. The size of the region was limited by the area that could be surveyed by the UAS in one flight and was the result of a balance between the desired diversity of deposits and map spatial resolution (a factor of the height above ground of the UAS flight). For each flight, the two cameras were synched and set to capture an image every three seconds with a slightly forward-looking viewing angle of 10° off-nadir. We flew a series of adjacent back-and-forth swaths (i.e., a "lawnmower" flight pattern) over the survey region at approximately 150 m above ground level. Image overlap for both the visual and TIR images in both the flight direction and between flight lines was generally about 75%, with flight speed adjustments and varying ground elevation causing overlap for individual images to range from 50 to 90%.

We conducted three UAS flights with the TIR camera and measured the temperature change of the volcanic deposits in our study area due to solar heating. Solar heating rate is highest and the difference in heating rate among surfaces is most pronounced in the hours immediately following sunrise (Price, 1977). The UAS survey was conducted at Sierra Negra on October 22, 2018, and UAS take off times were at 7:11 am, 8:18 am, and 9:35 am local time (UTC-06) (Table 1). While two flights are sufficient to determine solar heating rate, three or more measurements provide higher accuracy and data redundancy. Each flight lasted approximately 24 min and an average of 450 images were acquired per camera per flight (Table 1). Sunrise on this day was at 5:44 am. Ideally when applying this technique, the first UAS flight should occur prior to sunrise to observe conditions with no solar heating. However, on this day fog was present at sunrise, preventing UAS flight but also limiting solar heating of the ground. We flew the first flight immediately as the fog cleared to minimize the effect of solar heating in our first thermal survey.

2.2. Photogrammetric processing

We applied structure-from-motion (SfM) photogrammetry to create DEMs and orthophotos from the images taken during UAS flights (e.g., James and Robson, 2012; Bemis et al., 2014; James et al., 2019). We used Agisoft Metashape® version 1.5 for SfM processing. The location of each image tagged by the on-board GPS of the M210 provided the spatial information for the resulting models. The 'high' setting (In Metashape®, which means the images were processed at their original size, without downsampling) was used for both the initial alignment and generation of the dense cloud for all models. We generated orthophotos and DEMs for both the visual and TIR images from each flight. All products from SfM processing with Metashape® were exported with identical spatial resolution and boundary coordinates such that the pixel locations are identical for calculating the solar heating rate of the surface. Metashape® uses bilinear interpolation to vary the spatial resolution when exporting DEMs and orthophotos. We selected a spatial resolution of 0.20 m for these DEMs and orthophotos, based on rounding up from the lowest resolution temperature map of the three flights (Table 1).

2.3. Roughness

We calculated roughness from the DEM created from the visual images taken during the second of the three survey flights. This flight had better spatial coverage compared to the other two, and the visual images produced higher resolution DEMs and orthophotos compared to the TIR

Table 2
Classification regions. Solar heating rate (°C hr^{-1}) and roughness values for the 31 regions used to define the manual classification and as training data for the supervised machine learning classification (Fig. 6). The 'Simplified Classification' and 'Refined Classification' columns are the dominant surface type of each region for each classification based on visual observations in the field and inspection of the orthophoto (Fig. 1b) derived from the UAS images.

Region	Simplified Classification	Refined Classification	Heating Rate (°C hr^{-1})	Roughness (deg)
1	Tephra	Tephra	12.5	2.4
2	Tephra	Tephra	13.8	1.7
3	Tephra	Tephra	9.6	2.8
4	Tephra	Tephra	12.2	2.3
5	Tephra	Tephra	10.8	2.7
6	ʻAʻā	ʻAʻā – Ridge	5.0	4.3
7	ʻAʻā	ʻAʻā – Blocky	6.7	6.2
8	Pāhoehoe	Pāhoehoe – Crust	7.9	4.5
9	Pāhoehoe	Pāhoehoe – Crust	8.8	4.5
10	Pāhoehoe	Pāhoehoe – Crust	9.8	4.8
11	Pāhoehoe	Pāhoehoe – Crust	10.4	3.7
12	Pāhoehoe	Pāhoehoe – Crust	8.5	3.8
13	Pāhoehoe	Pāhoehoe – Crust	10.7	3.1
14	Pāhoehoe	Pāhoehoe – Slabby	9.2	7.1
15	Pāhoehoe	Pāhoehoe – Crust	9.6	4.5
16	Pāhoehoe	Pāhoehoe – Slabby	8.4	7.5
17	Pāhoehoe	Pāhoehoe – Slabby	8.5	7.9
18	Pāhoehoe	Pāhoehoe – Slabby	6.9	6.7
19	ʻAʻā	ʻAʻā – Ridge	6.8	4.3
20	ʻAʻā	ʻAʻā – Ridge	6.7	3.9
21	ʻAʻā	ʻAʻā – Ridge	6.1	2.3
22	ʻAʻā	ʻAʻā – Ridge	5.3	3.1
23	ʻAʻā	ʻAʻā – Blocky	4.1	6.9
24	ʻAʻā	ʻAʻā – Blocky	4.7	5.6
25	ʻAʻā	ʻAʻā – Blocky	6.0	6.1
26	ʻAʻā	ʻAʻā – Blocky	4.8	4.5
27	Pāhoehoe	Pāhoehoe – Slabby	7.0	7.3
28	ʻAʻā	ʻAʻā – Blocky	5.5	6.0
29	ʻAʻā	ʻAʻā – Blocky	7.7	5.2
30	ʻAʻā	ʻAʻā – Blocky	5.9	5.3
31	ʻAʻā	ʻAʻā – Blocky	5.0	4.1

images (Table 1). Following the workflow of James et al. (2020b), we estimated that the average vertical error of the DEM is 0.15 m. This suggests that the DEM is sensitive to elevation changes between neighboring pixels on the order of 0.1 m. From the DEM, we calculated the slope and aspect of the terrain. Following Grohmann et al. (2011), we calculated surface roughness as the standard deviation of the slope values within a 5 × 5 pixel moving window. This resulted in roughness sensitive to variations with a lateral extent on the order of 1 m (five pixels with 0.2 m spatial resolution).

2.4. Solar heating rate maps

Agisoft Metashape® is only compatible with integer digital number (DN) images. When the radiometric JPEG (joint photographic experts group) images from the Zenmuse XT are loaded into Metashape®, the temperature values are automatically converted to a single-band gray-scale 8-bit DN (DN values from 0 to 255). To create a photogrammetric model that we can correlate to temperature values, the images captured by the TIR camera must be uniformly converted to DN. We first used the ResearchIR® software from FLIR to convert all images to a tagged image format (TIF) file that could be read by Matlab® (among other software platforms). For each group of TIR images that would be used to create one photogrammetric model in Metashape® (in this case all the images captured during a single flight), we performed a linear scaling of the temperature values over the entire image set and converted to a 16-bit DN (DN values from 0 to 65,535). This conversion gives a DN value of 0 to the lowest temperature recorded in a pixel in any image in the set (T_{min}) and a DN value of 65,535 to the highest pixel temperature found in any image (T_{max}). The temperature for any pixel i in any image in the set (T_i) is then assigned a DN value by

$$DN_i = 65535 \times \left(\frac{T_i - T_{min}}{T_{max} - T_{min}} \right) \quad (3)$$

and DN_i is then rounded to the nearest integer. As the range between the maximum and minimum temperature in an image set for this study is < 130 °C (Table 1), each 16-bit DN value represents a step of < 0.002 °C. Given that the TIR camera has a sensitivity of < 50 mK (< 0.05 °C), the temperature scaling preserves the precision of the original measurement.

The linearly scaled DN images were loaded into Metashape® and processed as described in Section 2.2. We provided spatial reference using control points (markers) in Metashape® to align the temperature maps to the Flight 2 visual orthophoto. The control points were locations identifiable in both the visual and TIR orthophotos, and we used coordinates for the points derived from the visual orthophoto to ensure as precise an alignment of the temperature maps as possible. Using 17 controls points, we achieved sub-spatial resolution alignment accuracy (< 0.2 m) for all three temperature maps (Table 1). It is also possible (and common) to use a mapping GPS unit to survey control points and provide spatial reference for this type of UAS survey (James et al., 2019). However, we do not do this here because 1) distributing and measuring control points before the UAS survey was not ideal as it would have involved doing so in the dark (pre-sunrise) or leaving the control point markers in the field overnight and 2) this allows us to present a method that can be utilized in cases were surveying control points via GPS is similarly not feasible or impossible.

To produce the final temperature maps, we first exported the orthophoto created in Metashape® from the scaled images. Next, in Matlab®, we converted the 16-bit DNs back to temperature using the inverse of Eq. (3) (i.e., solving for T_i when knowing DN_i rather than solving for DN_i knowing T_i, as shown). Both the sensor measurement error and the SfM processing impact the accuracy of the temperature

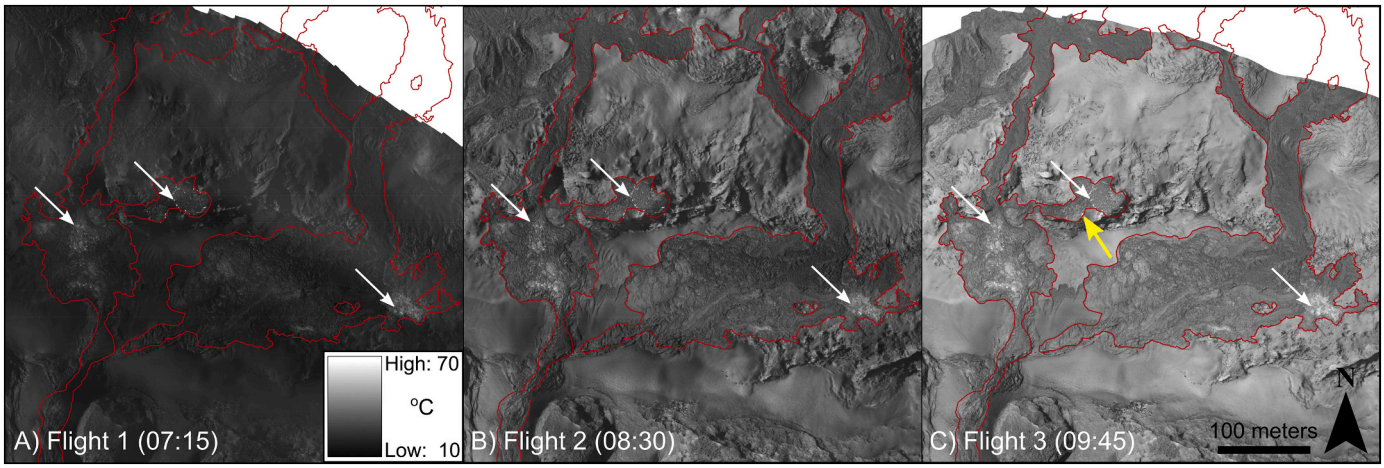

Fig. 2. Temperature Maps. The sequence of temperature maps (times are local, GMT-06) produced from the UAS TIR camera survey show differential heating of the land surface. The 2018 lava flows are outlined in red. Arrows highlight high temperature thermal anomalies associated with areas still releasing heat from the original eruption. The yellow arrow in (C) is the location of the highest temperature in any of the maps (115.3 °C). Data missing in the northeast corner of (A) and (C) is due to variations in the spatial coverage of the UAS flights. (For interpretation of the references to colour in this figure legend, the reader is referred to the web version of this article.)

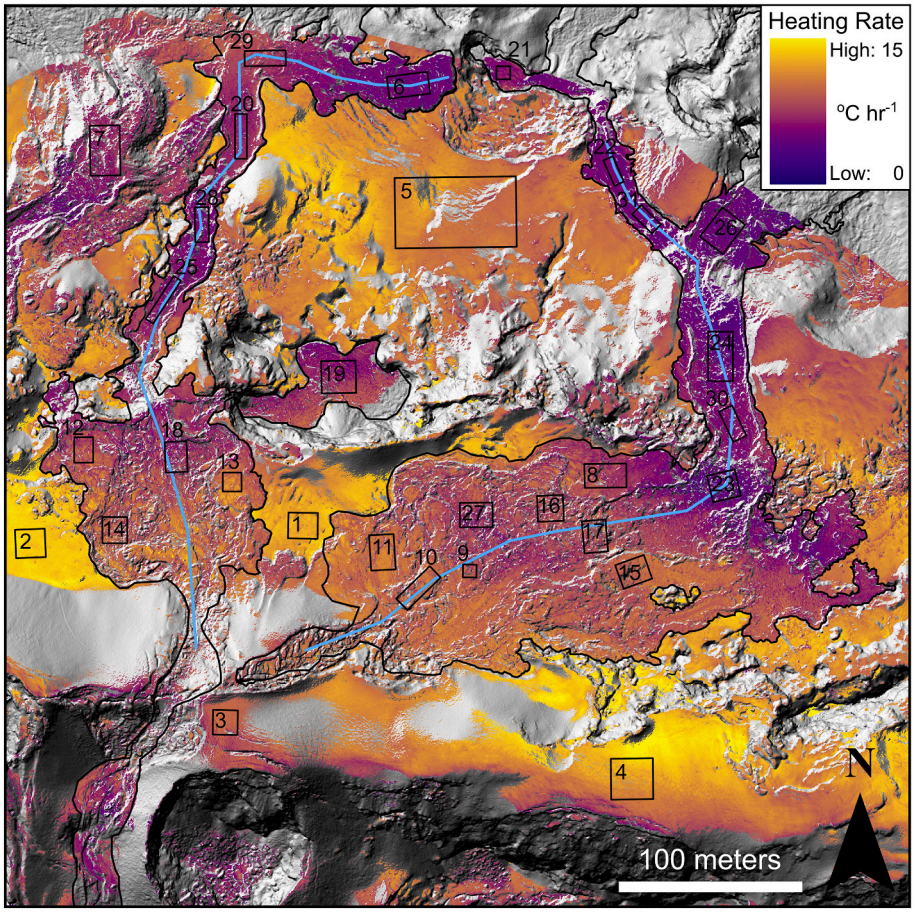

Fig. 3. Solar heating rate of Sierra Negra surfaces. The solar heating rate calculated from the three temperature maps shows high rates (yellow) in tephra-dominated surfaces and low rates (purple) for ʻaʻā lava. The basemap is a hillshade of the Flight 2 DEM. Areas with no solar heating rate data have a slope above 20° or were in shadow and were ignored to minimize the effect of surface reflectivity and preferential heating of a sloped surface facing towards or away from the rising sun. The blue line running down each flow branch is the profile line for Fig. 5. Numbered boxes are the regions used to define the manual classification. The 2018 lava flows are outlined in black. (For interpretation of the references to colour in this figure legend, the reader is referred to the web version of this article.)

maps. To generate an orthophoto from TIR images, Metashape® effectively averages the DN for a location as it appears in multiple individual images to produce a single value for the orthophoto. This will smooth details such as local maxima and minima but also minimize the effect of outlying values due to sensor measurement error (± 5 °C for the Zenmuse XT). For terrain with broadly uniform or gradual changes in surface temperature (such as our study area), the result is a temperature map with relative errors no larger than the measurement error in the images.

The solar heating rate for the surveyed region was calculated by fitting a linear best-fit line through the three temperature values for each pixel from the three temperature maps. We chose units for the solar heating rate of °C hr^{-1} for this study. To account for issues related to the surface reflectivity and preferential heating of a sloped surface facing

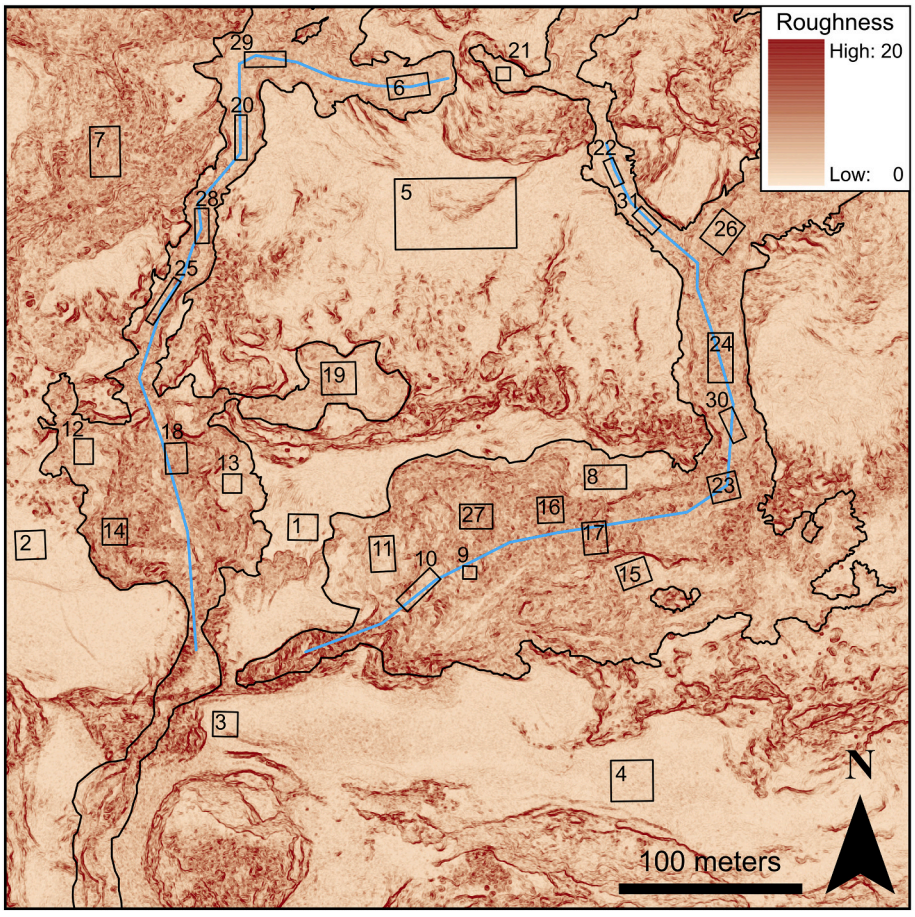

Fig. 4. Roughness of Sierra Negra surfaces. The surface roughness of the study area shows that the smoothest surfaces (lighter red) are tephra deposits and the roughest surfaces (darker red) are found near fissures and cliffs. Within the lava flow (black outline), the smoothest surfaces are pāhoehoe crust and the roughest are slabby pāhoehoe. The blue line running down each flow branch is the profile line for Fig. 5. Numbered boxes are the regions used to define the manual classification. (For interpretation of the references to colour in this figure legend, the reader is referred to the web version of this article.)

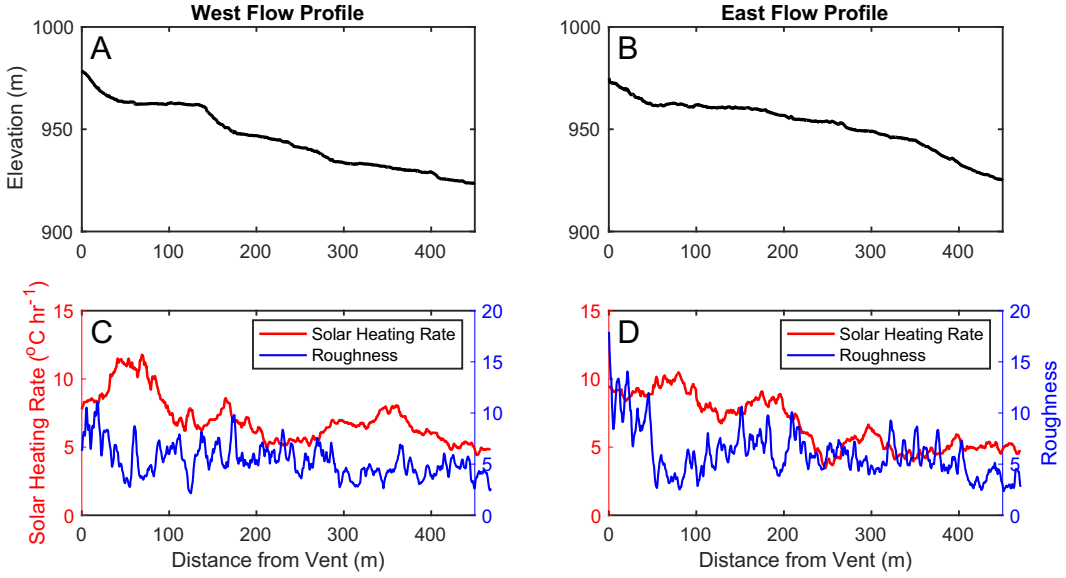

Fig. 5. Lava flow profiles. Downflow profiles of the elevation (A and B) and solar heating rate and roughness (C and D) are shown for the west (A and C) and east (B and D) flow branches in the study area. The profile line is shown in Figs. 3 and 4. Solar heating rate and roughness are plotted as 5 m running averages (25 pixels) to improve visualization by reducing noise and assigning a running average value to 'no data' locations. Solar heating rate shows a general decreasing trend downflow, with the lowest values associated with small breaks in slope (see at ~125 and ~ 225 m in the west profile and ~ 250 m in the east profile). Roughness does not show a strong trend downflow but is lowest near the vent where solar heating rate is highest (< 100 m downflow), associated with pāhoehoe crust surfaces.

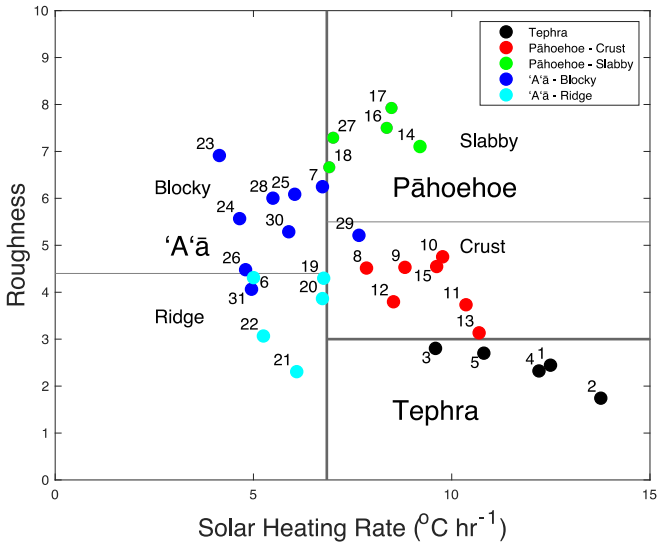

Fig. 6. Solar heating rate vs. Roughness for 31 training areas. The average solar heating rate and roughness for the 31 regions create a regime diagram for different surfaces. The gray lines in the diagram show the boundaries for each surface type used to define the simplified (thicker lines) and refined manual classifications. The colour of the dot for each region corresponds to the ground truthed surface type (see Fig. 1b). The ground truth surface type and the average solar heating rate and roughness for each region were used to as the training dataset for the supervised machine learning classification.

towards or away from the rising sun, we masked all pixels with a slope above 20 degrees. We also mask all pixels that are in shadow in the visual orthophoto (Fig. 1b) to account for decreased solar heating in these areas. The error in the solar heating rate is controlled by the variance of the temperature measurement error for each pixel in each map (a uniform error across all measurements does not affect solar heating rate). A two-point ΔT with a $\pm$ 5 °C measurement error could have an error as high as $\pm$10 °C, or 4 °C hr^{-1} for the 2.5 h of our measurements. Our use of a third temperature measurement to calculate solar heating rate reduces the effect of individual measurement errors. As the measurement error for each pixel in each map cannot be known to directly quantify the error, we assume the solar heating rate error to be < 4 °C hr^{-1}.

The solar heating rate values in the resulting map are best used as a measure of the relative thermal inertia of the different surface types in the study area. In addition to the properties of the surface, the solar heating rate is sensitive to numerous factors including ambient air temperature, cloud cover, season, and latitude. Thus, solar heating rate values are not directly comparable between different locations or different days, even for similar or identical surfaces. For future studies, a quantitative determination of ATI (Eq. 2) could be made possible through a more sophisticated methodology that includes estimating albedo. Albedo can be determined using either satellite-derived reflectivity data (e.g. Price et al., 2016; Simurda et al., 2020) or via UAS using a radiometrically calibrated sensor and a calibration target. We refrained from attempting this for this study as 1) we were interested in developing a simplified workflow that did not require extensive access to the survey area (e.g., for ground truth, ground control points, calibration targets, etc.), and 2) the highest spatial resolution satellite-

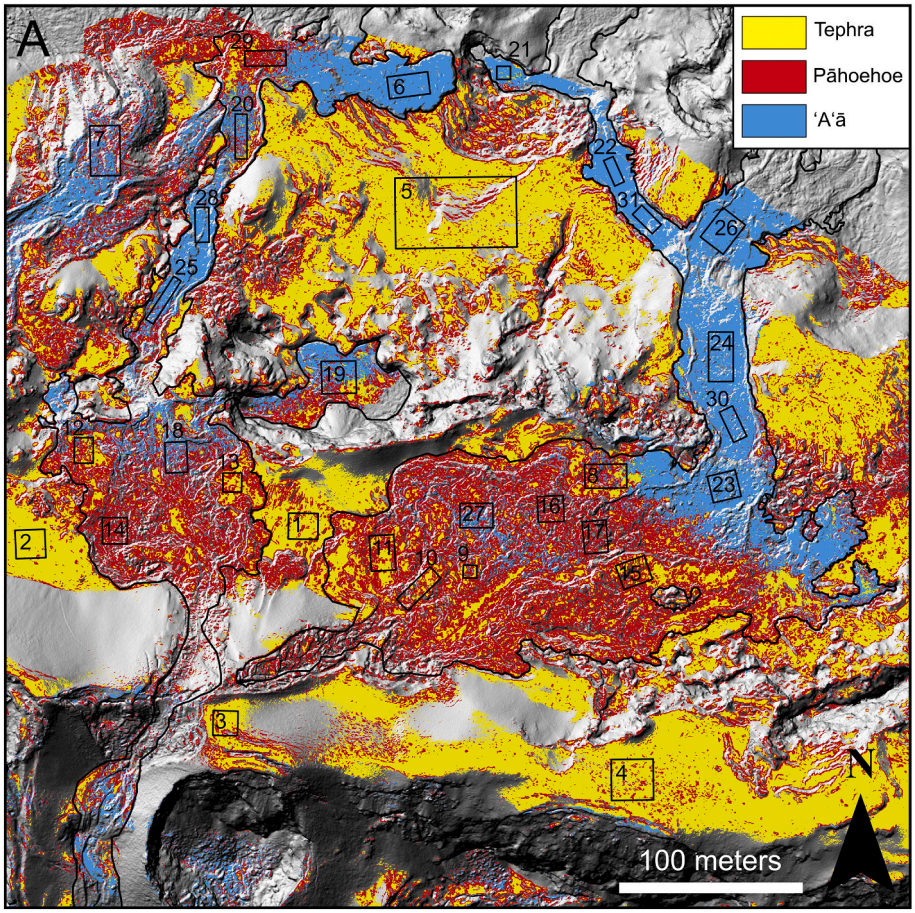

Fig. 7. Simplified classification. Surface types at Sierra Negra classified into three categories (tephra, pāhoehoe lava, and 'a'ā lava) based on manual (a), supervised machine learning (b), and unsupervised machine learning (c) methods.

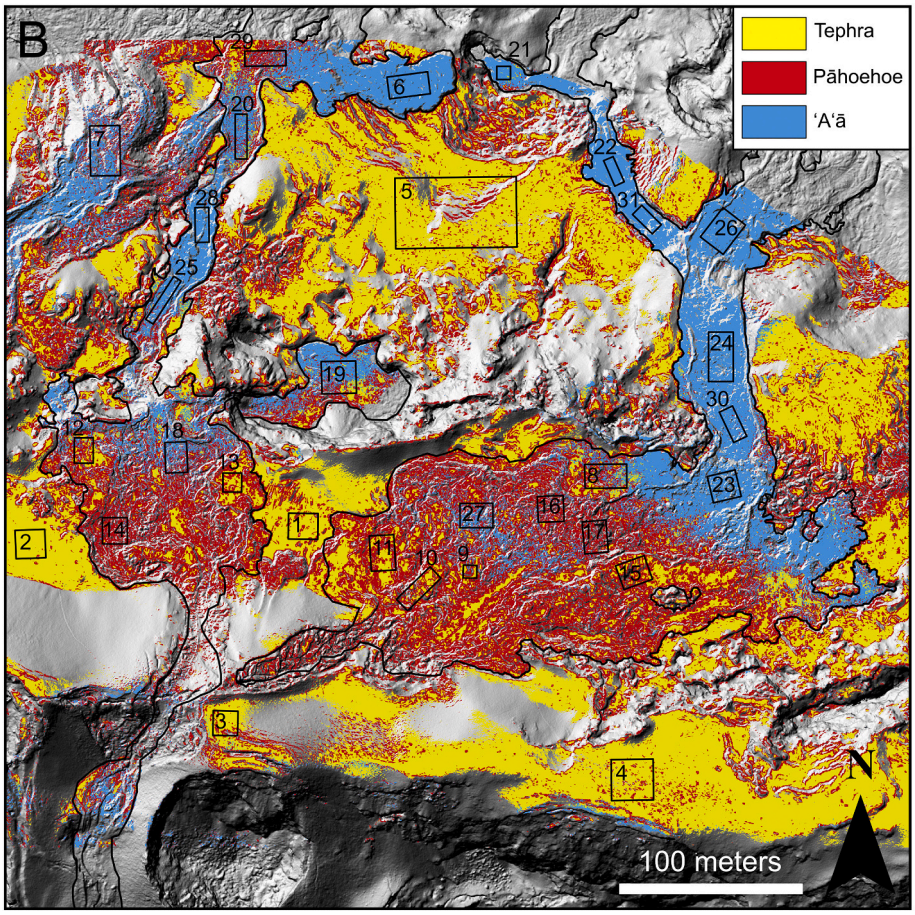

Fig. 7. (*continued*).

derived reflectance data is 90 m, which would cause sub-pixel mixing errors (Simurda et al., 2020) if applied to our 0.2-m spatial resolution data.

We also consider the contributions of sub-pixel roughness on the solar heating rate. As noted previously, Simurda et al. (2020) found that ATI does not perfectly correlate with particle size. Coarse sized particles did not yield the highest ATI because they produced sub-pixel shadows and trapped fine particles. At the scale investigated in our study (0.2 m), tephra of various sizes and small blocks of lava represent the fine, medium, and coarse particle sizes that influence sub-pixel roughness. Sub-pixel roughness due to variations in these particle sizes will not impact our lava classification methods because we do not anticipate widespread sub-pixel (less than 0.2 m) mixing of tephra, pāhoehoe lava, and ʻaʻā lava (see next section for additional details on our classification scheme). Additionally, if these variations are more prevalent than we expect, their effects will be accounted for in the classification technique. The classifications are based on variations in solar heating rate and roughness. Therefore, any significant variations in solar heating rate due to sub-pixel roughness will be included in our classification scheme.

2.5. Classification

We classified surfaces based on their roughness and solar heating rate using manual and machine learning techniques. We applied a simplified ($n = 3$) and refined ($n = 5$) classification of surface types that are most prevalent in the study area, based on field observations. In the simplified classification, these surfaces were tephra, pāhoehoe lava, and ʻaʻā lava. In the refined classification, these surfaces were tephra, pāhoehoe with intact crust, slabby pāhoehoe, blocky ʻaʻā, and ʻaʻā with visible surface ridges. The four categories of lava correlate roughly to the down flow progression of lava morphology which we observed (Fig. 1b) and the progression of lava morphologies described by Lipman and Banks (1987). Pāhoehoe with intact crust is located closest to the vent (pāhoehoe, Lipman and Banks, 1987). Slabby pāhoehoe occurs where the crust was fractured before the lava transitioned to ʻaʻā (slabby ʻaʻā or pāhoehoe, Lipman and Banks, 1987). The ʻaʻā with visible surface ridges (scoriaceous ʻaʻā, Lipman and Banks, 1987) is found in breakout lobes and some channelized portions of the flow (Fig. 1b) and has smaller surface clast sizes compared to the blocky ʻaʻā, (blocky ʻaʻā, Lipman and Banks, 1987). We observed blocky ʻaʻā downflow of the pāhoehoe-ʻaʻā transition and in the main channel of the eastern flow branch (Fig. 1b).

For the manual classification method, we first identified 31 'training' areas that contain only one of the surface types. We then calculated the average roughness and solar heating rate for each of these areas (Table 2 and boxes in Fig. 1b). These average values define regions in roughness-solar heating rate space, which provide the ranges of roughness and solar heating rate values associated with each surface type. We used these ranges to classify each pixel in the study area. As these regions represent a single surface type, the variation of roughness and solar heating rate values for the pixels within the regions provides a means to assess the significance of differences between the region averages. In general, solar heating rate is more uniform within a region compared to roughness. The standard deviation of the pixel values for each region suggests that differences in the average value between regions of 1 °C hr^{-1} for solar heating rate and 2 for roughness represent clear distinctions in surface characteristics.

We experimented with supervised and unsupervised machine learning methods for per-pixel classification of surface types, then tested the performance of these methods by comparing them to the manually classified maps. Supervised machine learning techniques have proven

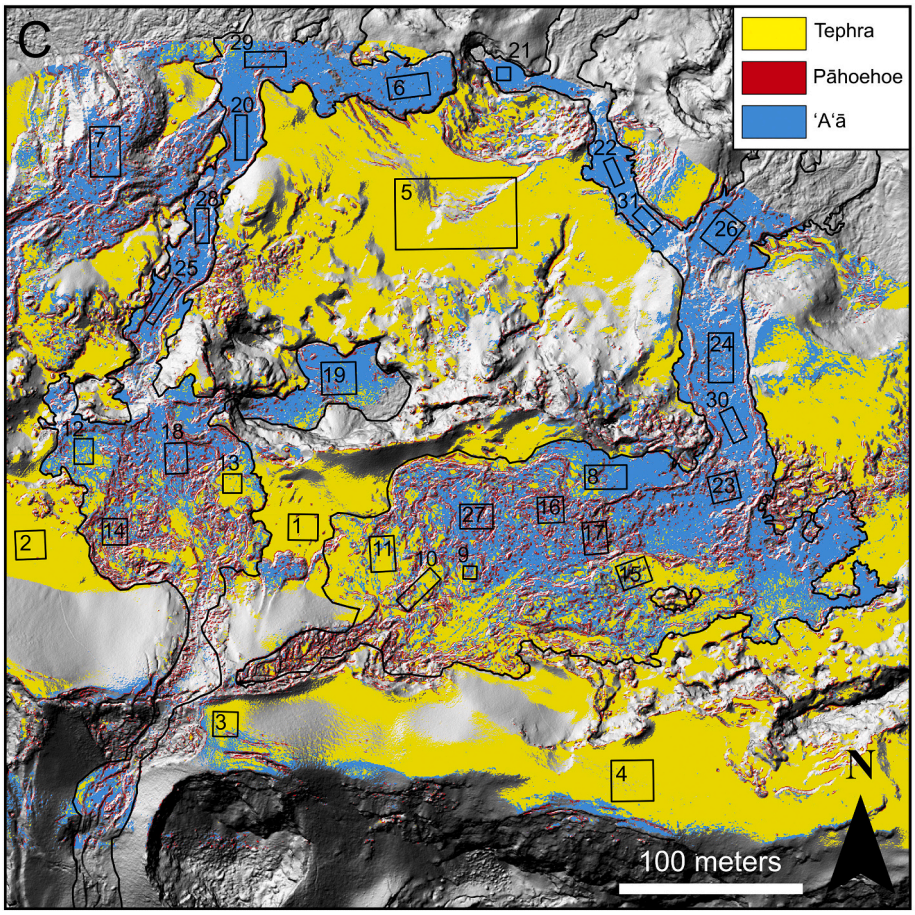

Fig. 7. (*continued*).

successful at efficiently mapping volcanic deposits in remote imagery (e.g., Li et al., 2017; Corradino et al., 2019). Similar to previous works (e.g., Waske et al., 2009; Kereszturi et al., 2018),

we used a random forest algorithm trained on the manually identified training areas to classify each pixel in the image as one of the three (or five) surface types. We carry out this step using the `scipy.ensemble.RandomForestClassifier` Python package (Pedregosa et al., 2011).

We also explored unsupervised machine learning, used to recognize patterns within large datasets without training data. Unsupervised methods are thus beneficial for classifications in regions where field observations may not be possible, or where previous knowledge of the existing surface deposits may be limited. We used a k-means algorithm to identify discrete clusters of pixels grouped in roughness-solar heating rate space, which we then interpreted as different surface types. We chose to use three (or five) clusters to match the manual simplified and refined classifications. We performed the k-means clustering using the `scipy.cluster.KMeans` Python package (Pedregosa et al., 2011).

3. Results

The three temperature maps generated from the UAS TIR images show surfaces heating at different rates as solar input increases within the sequence (Fig. 2). In the latest image (Fig. 2c, most solar input), the lava flows appear notably cooler than the surrounding terrain. Small, high-temperature thermal anomalies (white arrows, Fig. 2) indicate that in areas where the lava ponded or was emplaced at a greater thickness, the flow was still cooling four months after the eruption. The highest temperature observed in any of the maps is 115.3 °C (yellow arrow, Fig. 2c), located along a crack in the lava flow surface in an area where lava ponded in a crater.

The solar heating rate of the land surface in the study area shows several consistent patterns (Fig. 3). The highest solar heating rates are found where tephra is the dominant surface type (compare Fig. 3 to Fig. 1b). Variations in the solar heating rate of tephra are primarily related to the slope and aspect of the surface- flat and/or east-facing (sun-facing) slopes have generally higher solar heating rate than steeper and/or west-facing slopes. The effect of slope on the solar heating rate in tephra deposits can be seen in Fig. 3 near Region 4 where solar heating rate decreases smoothly to the south as the slope increases towards the caldera rim. The lowest solar heating rate found in tephra deposits is in Region 3 (Fig. 3), near a vent from the 2018 eruption. The solar heating rate generally decreases down the length of the lava flows as flow morphology transitions from initially pāhoehoe near the vent to ‘a‘ā. The highest solar heating rates on the lava flow surface are found near the vent where intact pāhoehoe crust is present (Fig. 1b; Fig. 3). The lowest solar heating rate within the flow is located where the lava flows over a ‘step’ where the slope is greater (Region 23, Fig. 3).

The meter-scale surface roughness of the study area (Fig. 4) shows that tephra surfaces are the smoothest. The roughest lava flow surface is fractured pāhoehoe crust near the transition to ‘a‘ā (Regions 16 and 17, Fig. 4), with intact pāhoehoe crust and ridged ‘a‘ā both appearing smoother (Regions 13 and 6, Fig. 4). Directly comparing the roughness and solar heating rate along two flow profiles (Fig. 5) shows the general decrease in solar heating rate with distance downflow.

We calculated the average solar heating rate and roughness for the 31 regions shown in Figs. 3 and 4 (Table 2) and plot them against each other in Fig. 6. These regional average values define the training data for the supervised machine learning classification. The gray lines in Fig. 6 indicate the boundaries between surface types used to define the manual

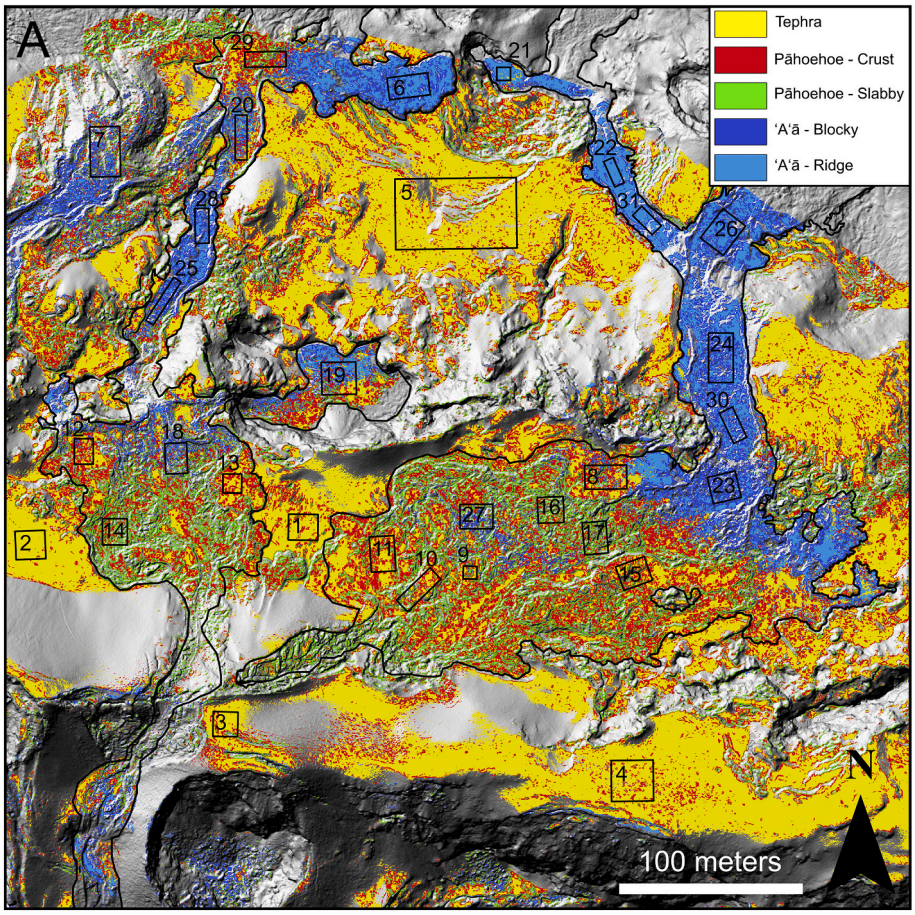

Fig. 8. Refined classification. Surface types at Sierra Negra classified into five categories (tephra, pāhoehoe crust, slabby pāhoehoe, blocky ʻaʻā, and ridged ʻaʻā) based on manual (a), supervised machine learning (b), and unsupervised machine learning (c) methods.

classification. In general, lava is distinguished from tephra by roughness. In the case where an ʻaʻā region has a roughness similar to tephra (due to a scoriaceous texture with tightly packed, smaller blocks that created a relatively smooth surface), it is distinguished by its slower solar heating rate (Region 21, Fig. 6). Pāhoehoe and ʻaʻā lava morphologies are primarily separated by the solar heating rate (Fig. 6). In the refined classification (five surface types), the distinction between morphologies of ʻaʻā (blocky and ridge) and pāhoehoe (crust and slabby) is based on the roughness (Fig. 6); there is no discernable difference in the solar heating rate for these lava morphologies. The proximity of many regions to the boundary lines indicates that there is a gradual, rather than a sharp, distinction between morphologies in these data. This proximity will also cause some misclassification of surfaces, as the difference in roughness and solar heating rate values between regions are less than the variability in the values of the pixels within the regions, as defined by the standard deviation of pixel values in the region (Supplemental Fig. S1).

The range of roughness and solar heating rate values used for the manual classification are: tephra (roughness < 3; solar heating rate $>$ 6.85); pāhoehoe (roughness > 3; solar heating rate > 6.85); ʻaʻā (any roughness; solar heating rate < 6.85); pāhoehoe-crust ($3 <$ roughness $<$ 5.5; solar heating rate > 6.85); pāhoehoe-slabby (roughness > 5.5; solar heating rate > 6.85); ʻaʻā-ridge (roughness < 4.4; solar heating rate $<$ 6.85); ʻaʻā-blocky (roughness > 4.4; solar heating rate < 6.85).

The results of the manual classification applied to every pixel in the study area (Fig. 7a and 8a) show good qualitative agreement with our field observations (Fig. 1b). For the simplified classification (three surface types), the eastern flow branch shows a clear transition from pāhoehoe to ʻaʻā lava approximately 200 m downflow from the vent (red to blue change between Regions 17 and 23, Fig. 7a). The transition to ʻaʻā in the western flow branch is less defined and a large pāhoehoe component is present downflow near Region 29. In addition to the 2018 eruption deposits, this classification also identifies an older ʻaʻā lava flow to the west (Region 7, Fig. 7a). Some surface area outside of the lava flows is classified as pāhoehoe (red areas around Region 5, Fig. 7a) and is mostly associated with changes in slope (i.e., ridges, fissures, and other rock outcroppings that increase roughness) in tephra-dominated regions (yellow). Very little area outside of the lava flows is classified as ʻaʻā. Some areas of smooth pāhoehoe crust are also classified as tephra because of their lower roughness (yellow area near Region 11, Fig. 7a).

The refined classification (Fig. 8a) is considerably noisier than the simplified classification (Fig. 7a) and does not show any clear pattern in the presence of lava morphologies in the flow. Slabby pāhoehoe is particularly poorly classified. Due to the 0.2 m spatial resolution of the input maps, the refined classification is better at identifying the edges and surfaces of individual pāhoehoe crust blocks (areas surrounding Regions 14 and 16, Fig. 8a) than the broad region of slabby pāhoehoe morphology (Fig. 1b). Similarly, for ʻaʻā, the refined classification is better at identifying individual ridges (Region 6, Fig. 8a) or levees (to the west of Region 24, Fig. 8a) than it is broad areas of the flow surface where ridged or blocky morphology is present.

For three surface categories, machine learning methods, both supervised and unsupervised, can efficiently replicate the manual classification (Fig. 7). Because it was trained on the 31 manually classified regions, the supervised (random forest) method very closely resembles the manual method (compare Fig. 7a and b). The unsupervised (k-means) method identifies tephra and ʻaʻā lava with minimal

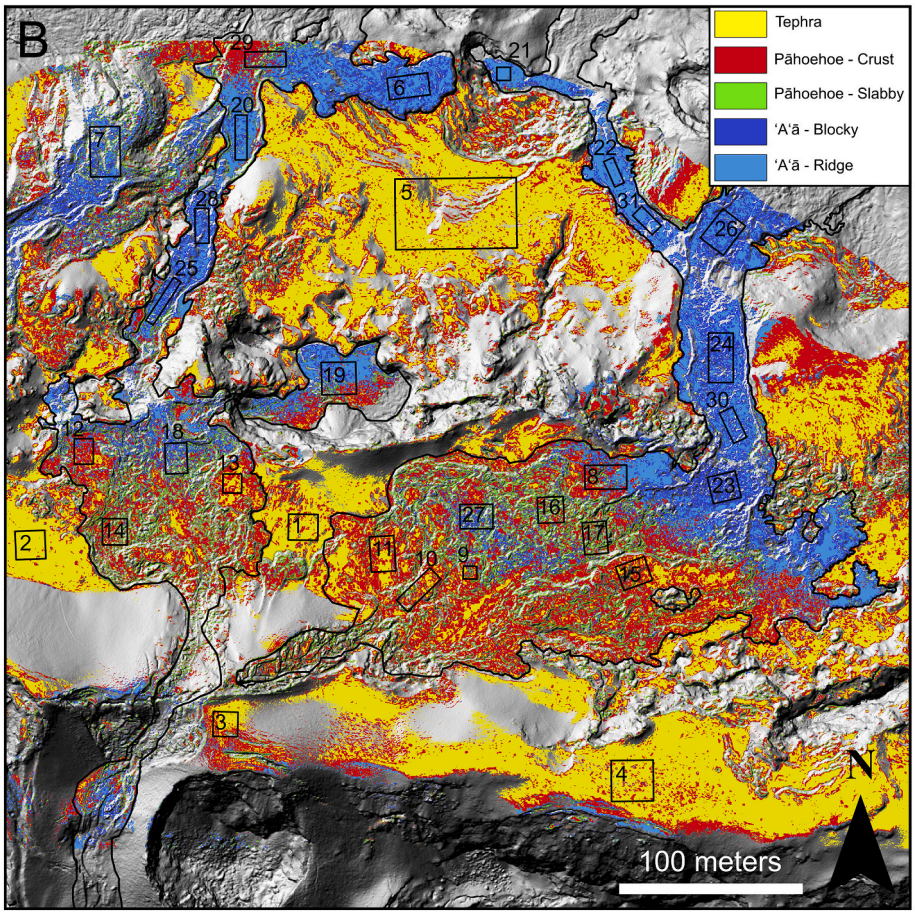

Fig. 8. (*continued*).

misclassification compared to the manual and supervised machine learning method (compare Regions 5 and 29 in Fig. 7a and c). However, the unsupervised method is unable to broadly identify pāhoehoe lava. The near-vent pāhoehoe-dominated region of the lava flow is absent, with pāhoehoe-classified pixels limited to the edges of crust blocks (Fig. 7c).

Results from the refined machine learning classifications are mixed. Supervised machine learning can differentiate between the manually defined surface types, with the map having similar appearance to the manual classification (Fig. 8a and b). However, the refined supervised classification is worse at distinguishing tephra and pāhoehoe compared to the simplified supervised classification (Figs. 7b and 8b). The unsupervised method, with no training data to guide it, deviates from our visually defined categories (Fig. 8c). The ʻaʻā lava (dark blue, Fig. 8c) remains a single surface type and appears similarly to the ʻaʻā regions in the simplified classifications (Fig. 7). Tephra is split into two categories (yellow and red, Fig. 8c) with the difference appearing to be based on the slope and aspect of the surface. These two tephra categories also include most of what we visually identified as intact pāhoehoe crust (Regions 10 and 11, Fig. 8c). Light blue pixels correlate with extremely high roughness at sharp edges but are relatively few in number compared to other categories and difficult to identify in Fig. 8c. However, slabby pāhoehoe is identified with reasonable accuracy (Regions 14, 16, and 17, Fig. 8c). In general, the refined unsupervised classification is poor and not able to identify categories that correspond to visually distinct surface morphologies.

The patterns discussed above are represented quantitatively in the confusion matrices in Fig. 9. In these plots, the ‘true label’ is the manual classification and the ‘predicted label’ is the machine learning classification. The number in each square is the fraction of the pixels in a ‘true’ category that are found in a given ‘predicted’ category. For example, in Fig. 9a, 93% of pāhoehoe pixels in the manual classification were also classified as pāhoehoe by the supervised random forest method. For the simplified classification, the supervised method classifies all categories with greater than 90% accuracy (Fig. 9a). The unsupervised method’s difficulty in classifying pāhoehoe is clearly shown (Fig. 9b), with only 21% of manually classified pāhoehoe pixels correctly predicted, compared to 92% and 83% accuracy for tephra and ʻaʻā, respectively. For the refined classification, the supervised method classifies all categories with 84–88% accuracy except for slabby pāhoehoe, which is 61% (Fig. 9c). The confusion matrix for the unsupervised refined classification (Fig. 9d) confirms the patterns observed in the classification map (Fig. 8c), where both the blocky ʻaʻā (99%) and ridged ʻaʻā (79%) were classified as blocky ʻaʻā, and tephra was split nearly evenly into two categories (54% and 46%). The unsupervised method is superior to the supervised method in classifying slabby pāhoehoe however, doing so with 74% accuracy.

4. Discussion

4.1. Using solar heating rate and roughness to describe volcanic deposits

Roughness and solar heating rate describe inherently different surface properties. Roughness, as a measurement of the surface texture, is better at distinguishing morphological differences in volcanic deposits. This is shown by the separate morphologies of pāhoehoe (crust and slabby) and ʻaʻā (ridge and blocky) lava in the refined classification having essentially no difference in solar heating rate but variable roughness (Fig. 6). Solar heating rate, which is inversely related to thermal inertia (Eq. 1; Eq. 2), is a measurement of physical properties of

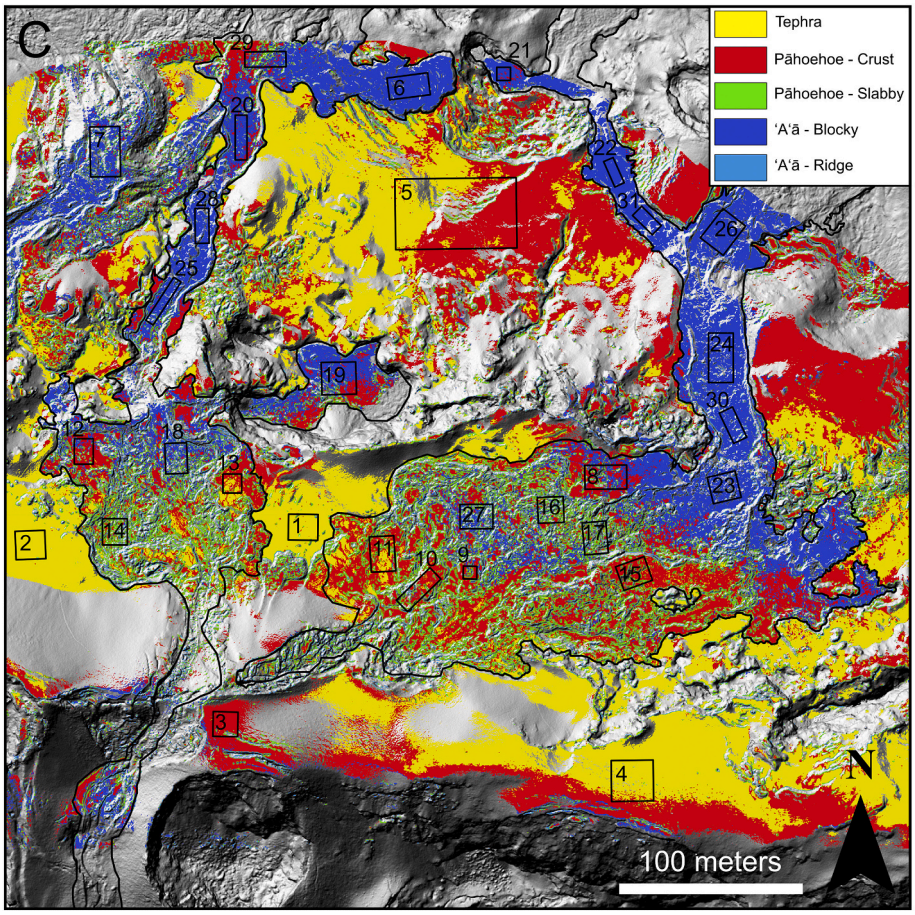

Fig. 8. (*continued*).

the deposit. In this study that primarily refers to the grain size and density. However, solar heating rate also includes the effects of sub-pixel roughness: roughness that is below the scale of the measured roughness that was discussed above. We have determined that solar heating rate is an excellent method for discriminating between the major depositional types (i.e., tephra, pāhoehoe, and ʻaʻā) in the study area (Fig. 3; Fig. 6).

Tephra is generally distinct from the lava due to its smaller grain size compared to the blocks and crust of the lava flow (Fig. 3; Fig. 6). Similarly, Price et al. (2016) also found that tephra had lower ATI (i.e., higher solar heating rate) compared to lava. While solar heating rate should be sensitive to variations in the clast size of tephra deposits, we did not visually observe in the field any significant clast size variations in regions where gradients in the tephra solar heating rate are visible (near Regions 4 and 5, Fig. 3). We thus attribute these gradients to the influence of the slope and aspect of the surface, which likely overwhelms minor variations in tephra clast size. One possible exception to this is observed when comparing Region 3 (near vents from the 2018 eruption) to Region 4 (200 m to the east) (Fig. 3; Fig. 6; Table 2). Both regions have similar slope and aspect, yet the near-vent Region 3 has the lowest solar heating rate (and highest roughness) of any tephra region (Fig. 6; Table 2). We observed relatively larger clasts of tephra and spatter surrounding the vents, so clast size is a possible explanation in this case for the difference in solar heating rate. We do not have quantitative clast sizes for the tephra studied in this area.

The downflow decrease in solar heating rate that we observe at Sierra Negra is likely a result of increasing density of the lava (decreasing vesicularity) due to degassing as it flowed downslope. This pattern is well-described for other lava flows (e.g., Lipman and Banks, 1987). Lava density may also explain the solar heating rate and roughness we observe for the slabby pāhoehoe (Fig. 6). While the slabby pāhoehoe represents the roughest surface of the Sierra Negra lava flows (Fig. 4), the solar heating rate does not have correspondingly low values indicative of such large blocks. Rather, slabby pāhoehoe has intermediate solar heating rate between the pāhoehoe crust and ʻaʻā morphologies, a result of the higher vesicularity of this material compared to the ʻaʻā downflow (Fig. 3; Fig. 5d; Fig. 6). This intermediate solar heating rate could also be influenced by sub-pixel roughness. As demonstrated in Simurda et al. (2020), if the scale of the slabs in the slabby pāhoehoe are such that they introduce small (sub-pixel) shadows, this could raise the solar heating rate slightly. The precise relative effects of density and particle size on the solar heating rate for a material cannot be separated in this study.

The conditions that existed during lava flow emplacement can be interpreted based on where different lava flow morphologies are located. The pāhoehoe to ʻaʻā transition for both the east and west flows is located near an increase in slope (Fig. 5; Fig. 7). The steeper slope would have increased flow velocity and thus the strain rate within the lava, promoting the transition to ʻaʻā as the lava viscosity also increased with distance from the vent due to degassing and cooling. The ridged ʻaʻā, with higher heating rate and lower roughness (i.e., lower density and/or smaller blocks) compared to the blocky ʻaʻā, is preferentially located in flow lobes away from the main channel (Regions 6, 21, and 22, Fig. 8). This suggests the ridged ʻaʻā regions were emplaced with lower viscosity earlier in the eruption, whereas the blocky ʻaʻā morphology in the main channel is likely due to dense, higher viscosity lava emplaced as the eruption rate decreased and the flow came to a stop.

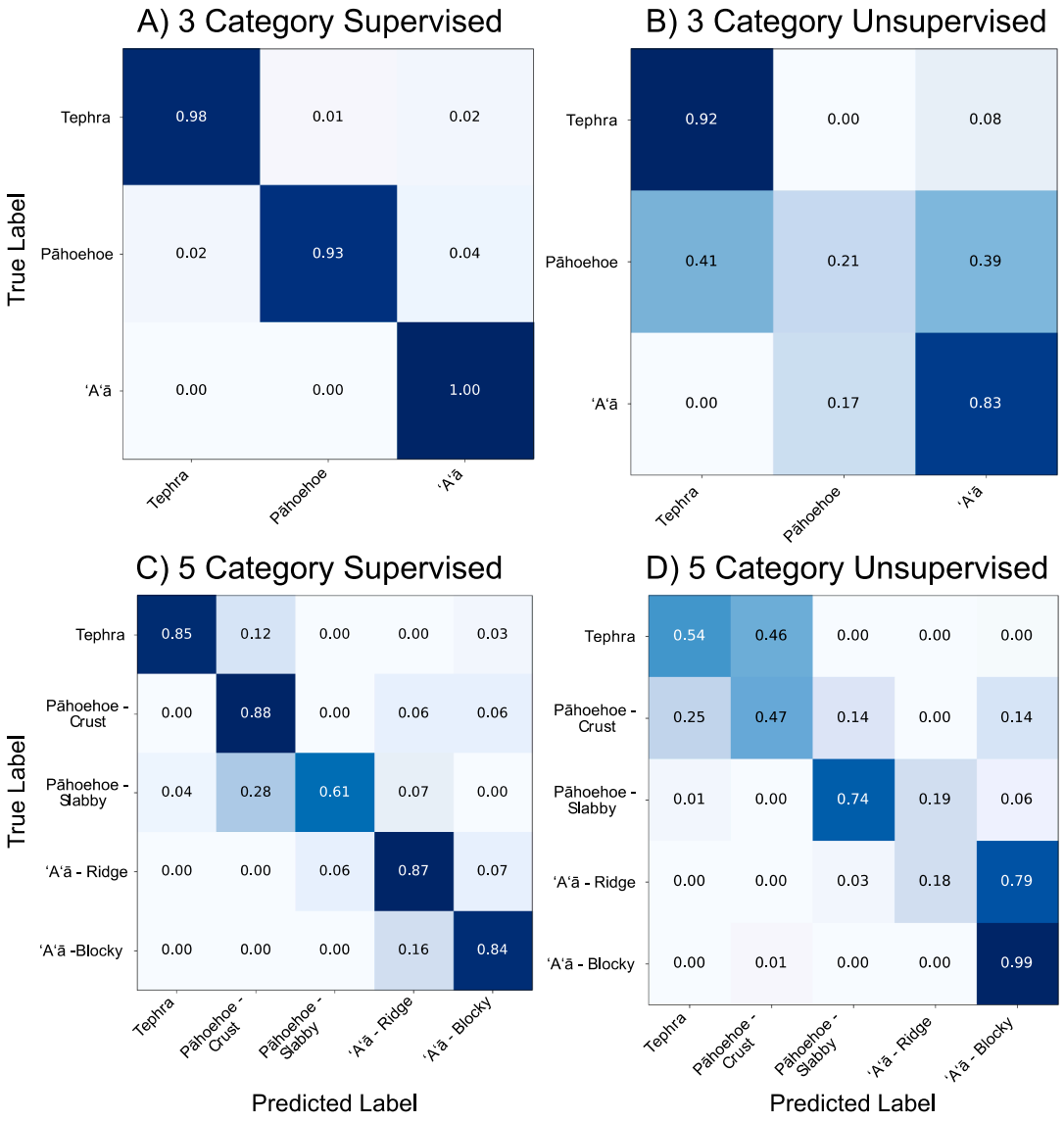

Fig. 9. Confusion matrices for machine learning classifications. Each matrix element displays the fraction of manually classified pixels ("true label") found in a given machine-learning-predicted category ("predicted label"). Dark colours on the diagonals indicate overall accurate predictions. For example, in (A), 100% of "'a'ā" pixels in the manual classification were predicted to be "'a'ā" by the supervised random forest method (A: three-category (supervised) random forest; B: three-category (unsupervised) k-means; C: five-category random forest; D: five-category k-means).

4.2. Classification accuracy

Investigation of the areas of apparent misclassification demonstrates the capabilities (or limitations) of our classification methods and identifies localities with complex deposits. For example, all classification methods we applied successfully identified an older lava flow as having 'a'ā morphology (Region 7, Fig. 7). This indicates our classification by roughness and solar heating rate does not distinguish between similar deposits of different ages (at least for age differences on the scale of decades). This is advantageous for mapping flow field morphology and extent surrounding a vent (or vents) but can be a hindrance for mapping a specific flow within a flow field if its extent is not known. Many surfaces outside of the 2018 flows which are classified as pāhoehoe are also not necessarily misclassified but are locations where older pāhoehoe surfaces are exposed within the tephra deposits (Fig. 7). Segments of pāhoehoe crust are often misclassified as tephra (yellow areas near Regions 11 and 13, Fig. 7), but in areas near the vent, the classification is correctly identifying tephra mantling the pāhoehoe crust (southwest of Region 11, Fig. 7). A section of 'a'ā lava in the northern part of the western flow segment (Region 29, Fig. 7) is misclassified as pāhoehoe due to a higher solar heating rate than is typical for 'a'ā (Fig. 3; Fig. 6). From the visual UAS images, block sizes in the flow appear smaller in this location and this is the likely cause of the increased solar heating rate. Interestingly, this area corresponds to a part of the 2018 lava flow that flowed over an 'a'ā flow from a previous eruption, suggesting that the roughness of the substrate over which lava flows may affect the block size of the lava. This is expected, since small-scale bed roughness impacts the flow advance rate and thus the balance between shearing and cooling timescales and the resulting flow morphology (Rumpf et al., 2018).

Both the manual and machine learning classifications highlight differences in how field identification of units differs from per pixel classification in remote sensing data. For example, it is straightforward to visually identify the pāhoehoe sections of the lava flow, yet all classification methods had difficultly identifying both pāhoehoe and the crust and slabby sub-morphologies (Fig. 9). The low accuracy of the unsupervised machine learning methods demonstrates that pāhoehoe is not identifiable as a single cohesive unit compared to other features in the

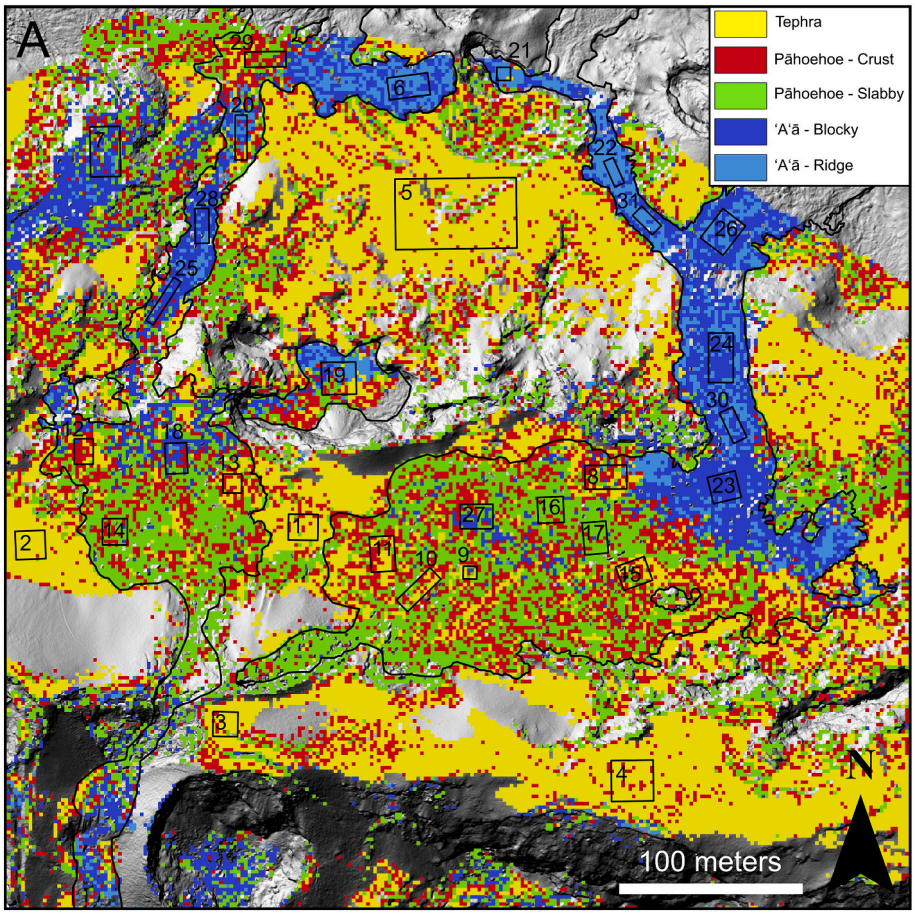

Fig. 10. Effect of reduced spatial resolution on classification. The manual refined classification (Fig. 8a) resampled to 2 m (A) and 20 m (B) spatial resolution. At 2 m resolution, the dominant morphology for different segments of the lava flow is potentially easier to identify compared to the original 0.2 m resolution. A resolution of 20 m is too coarse to clearly identify the flow margins and classification errors are more prominent.

study area (Fig. 7c; Fig. 9c). Similarly, while ʻaʻā is broadly identifiable as a distinctive unit by all classification methods (Fig. 7), the differences in roughness and solar heating rate between the visually identified blocky and ridged surface morphologies are not significant to the unsupervised machine learning method (Figs. 8c and 9d). Including the visual orthophoto as an additional component of the classification may be a means to improve pixel-by-pixel classification of lava flow morphology, as the properties of visual images may more directly correlate to how deposits are manually identified in the field (Soule et al., 2019).

Overall, the supervised method classifies lava surface types with an accuracy of 96% and 82% for the simplified and refined classifications, respectively, demonstrating its usefulness as an efficient and semi-automated mapping tool. The unsupervised machine learning method delivers a 61% and 55% accurate classification when compared to the manual simplified and refined classification maps, respectively. The unsupervised method's loss in per-pixel accuracy relative to supervised method makes it inadequate for mapping the different lava flow morphologies targeted in this study. However, Fig. 7c shows how the unsupervised k-means clustering can distinguish between tephra and the lava flow as a whole, independent of a priori knowledge about the deposits. The overall efficient mapping abilities of the unsupervised machine learning method is thus useful in cases where identification of major surface types without training data is desired. The manual and supervised machine learning classification techniques are best suited for applications looking to identify and map a specific deposit (or suite of deposits), as these methods allow the user to define the values of roughness and solar heating rate that apply to the surface(s) of interest.

4.3. *Effects of spatial resolution on classification*

A key factor that may account for the difference in visually identified units (Fig. 1b) and the classification techniques (Figs. 7 and 8) is the spatial resolution of the data. Whereas the eye can generalize across broad sections of terrain, our classification methods cannot and are limited to the 0.2 m resolution of the DEM and temperature maps. This is especially evident in the noisy appearance of the refined classification (Fig. 8), which identifies lava flow morphology varying on the order of meters rather than the 10s–100s of meters scale variations that we identified in the field (Fig. 1b). The 31 training regions (Table 2; Fig. 6) represent a classification based on a larger spatial resolution. The variations within each region are averaged out and result in a clear distinction between the intact crust and slabby pāhoehoe (Fig. 6) that is not seen in the classification maps (Fig. 8).

To test the effect of spatial resolution on the classification result, we resampled the manual refined classifications to a resolution of 2 m and 20 m (one and two orders of magnitude larger than the 0.2 m UAS dataset). The resampled pixel classification was determined by the most common surface category (i.e., the mode) among the 0.2 m resolution pixels contained within the new, larger pixel (Fig. 10). The 2 m resampled classification map (Fig. 10a) shows a reduction of noise within the lava morphologies compared to the original classification (Fig. 8a). The slabby pāhoehoe region is more clearly identifiable (Regions 16 and 17, Fig. 10a), but pāhoehoe crust is less distinct due to the

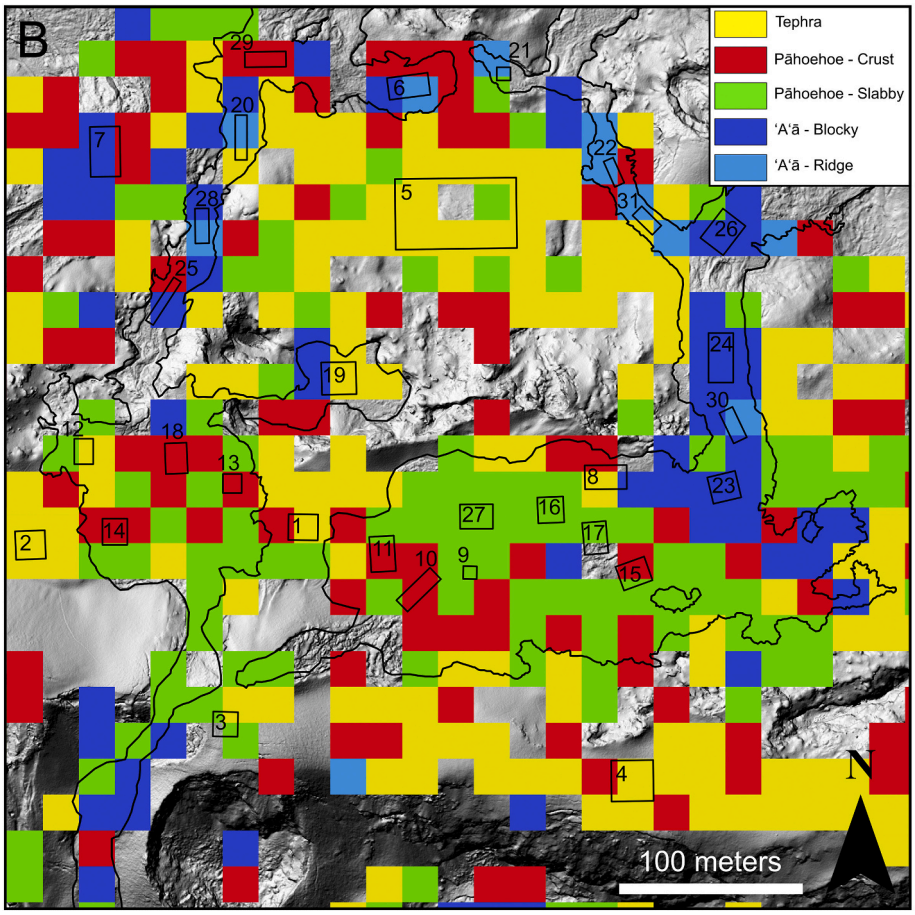

Fig. 10. (*continued*).

prevalence of smooth crust surfaces that were misclassified as tephra (Regions 10 and 11, Fig. 10a). It is easier to see that the main eastern channel has a dominantly blocky 'a'ā morphology (vicinity of Region 24, Fig. 10a), whereas the western branch of this channel is dominantly ridged 'a'ā (vicinity of Region 22, Fig. 10a). Downflow trends become harder to distinguish as the resolution approaches the width of the lava flow (Regions 22 and 28, Fig. 10b). Fig. 10 suggests that the ideal spatial resolution to use for classification in this context should be approximately an order of magnitude smaller than the scale of the identified units. If a unit has dimensions of 10s of meters (e.g., a 50 m wide lava flow), the spatial resolution should be on the order of a few meters to identify it clearly. This will reduce issues related to both classification on too fine a scale as described here and sub-pixel mixing of surface types when spatial resolution exceeds the scale of the features of interest (i.e., the failure of the surface uniformity assumption) as described by Simurda et al. (2020).

While we do not examine this in detail here, we also acknowledge that varying the spatial resolution of the input data (i.e., the UAS-derived DEM and temperature maps) changes the scale of feature to which the surface roughness is sensitive and the detail of variation in the solar heating rate. This potentially alters what the resulting classification map can show. The desired goals of the mapping and classification, and the spatial resolution required to achieve those goals, are important considerations when designing the initial UAS survey.

4.4. Application to other types of volcanic deposits

Surface solar heating rate and roughness can be used to classify many types of deposits in addition to those discussed so far. We conducted a similar UAS survey to the one described here at Sinabung Volcano (North Sumatra, Indonesia) (Supplementary Table S1). Starting in late 2013, an effusive eruption at Sinabung emplaced a 3 km long andesite lava flow and generated hundreds to thousands of PDCs caused by both lava dome collapse and Vulcanian-style explosions (Nakada et al., 2019). The deposits from the eruption cover approximately 10 km^2 (Pallister et al., 2019). We flew our dual-sensor UAS over a region of the northeastern part of the PDC deposits measuring approximately 2 km north-south and 1 km east-west. We captured TIR images during three flights before (335 TIR images), during (306 TIR images), and after (370 TIR images) sunrise (05:30, 06:30, 07:30 local time, GMT + 07) on July 6, 2018 (Supplementary Table S1). We created three thermal maps with 1-m spatial resolution (Supplementary Fig. S2), from which we calculated the solar heating rate (Fig. 11a). We used 323 visual images captured during two flights on July 8, 2018 to create an orthophoto and DEM.

Compared to the solar heating rate at Sierra Negra, the solar heating rate at Sinabung is minimal and broadly uniform (note the scale of Fig. 3 for Sierra Negra is from 0 to 15 °C hr^{-1} whereas the scale of Fig. 11a is from 0 to 3 °C hr^{-1}). The most notable feature in Fig. 11a is an area of relatively high solar heating rate in the center of the image. This area does not correlate with any variation in roughness or slope, which are all broadly homogenous at 1-m resolution for this region (Supplementary Fig. S3). We suggest that the higher heating rate in this location is due to a smaller average grain size. As a possible explanation for why smaller grain sizes are found in this area, we observe that the high heating rate correlates to a slight topographic high (Fig. 11b). This broad ridge is significant enough to affect the pattern of new drainage channels eroding into the pyroclastic deposits (note that channels are larger and denser to the north and west of the high heating rate area compared to the area visible in the orthophoto immediately to the northwest in

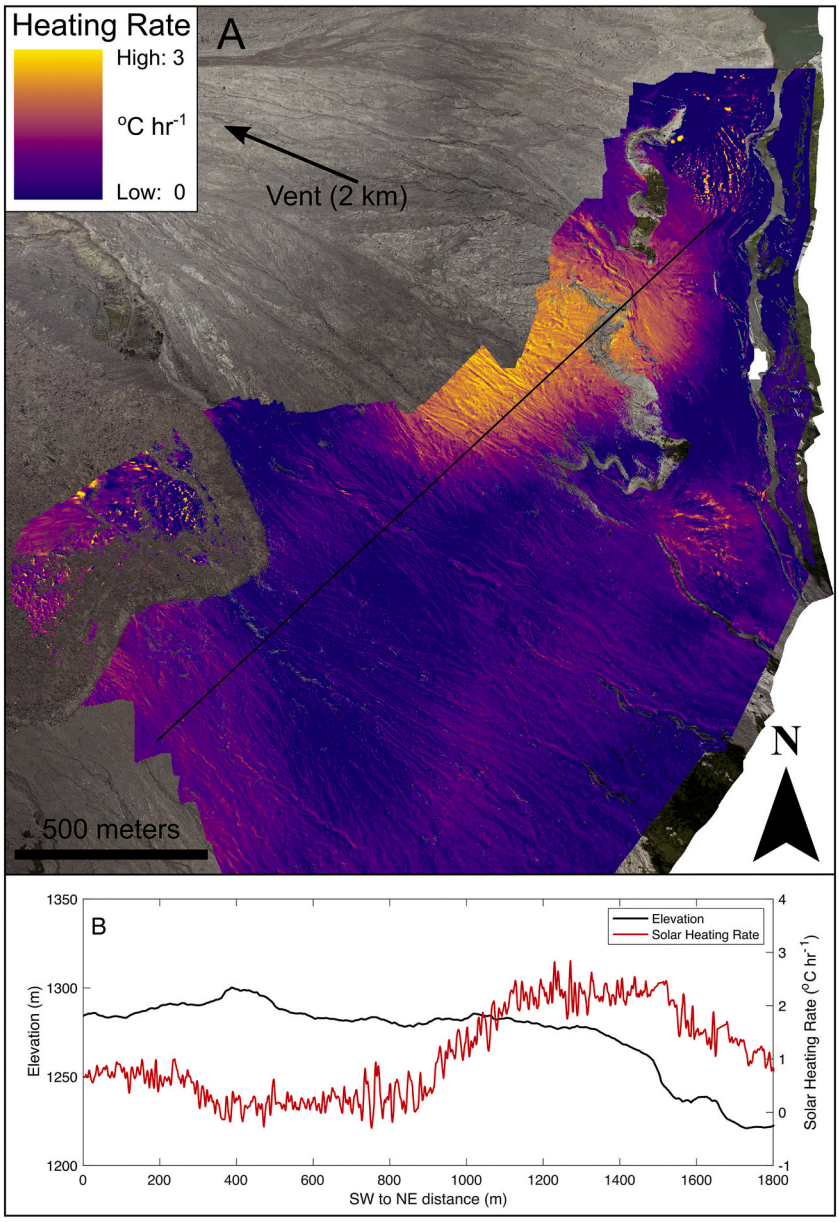

Fig. 11. Solar heating rate of pyroclastic deposits at Sinabung Volcano. The solar heating rate calculated for a region of PDC deposits at Sinabung Volcano (A) is generally uniform with minimal change across the scene except for a high-rate anomaly in the middle of the scene. The source region for the PDCs is located to the northwest, 2 km beyond the extent of the scene. The basemap is an orthophoto produced from visual images taken by a UAS. Comparing the solar heating rate and elevation along a profile line (black line, A) shows that the higher solar heating rate corresponds to a slight topographic high (B).

Fig. 11a). It is possible that this topographic high could have diverted more coarse-grained pyroclastic flows and led to the preferential deposition of finer-grained material in this area.

Near-zero solar heating rates are common near a river running north-to-south along the east side of Fig. 11a. Though it may not explain similarly low solar heating rate in other locations, these low values are potentially due to higher water content in the deposits near the river, which increases the thermal inertia (decreases solar heating rate) in materials. This reinforces the potential of UAS-derived solar heating rate to detect moisture content of surfaces, as was measured using satellite-derived ATI by Scheidt et al. (2010).

Ongoing activity at Sinabung prevented the ability to ground truth the region surveyed and any grain size variations that may exist are not obvious in visual inspection of the UAS images or the 0.5 m orthophoto we created. Additionally, understanding of the solar heating rate patterns observed would benefit from more data coverage to the north and west, but this was not possible due to the range of the UAS and safety considerations. We captured a portion of the lava flow in our data (far west center of Fig. 11a), but not enough to draw any conclusions related to the block size or density of the lava. Still, this application demonstrates two useful benefits of measuring surface solar heating rate for volcanic deposits. First, solar heating rate is more sensitive to grain size variations than roughness when spatial resolution exceeds the grain size. Second, measuring solar heating rate enables at least qualitative description of grain size variations in pyroclastic deposits while an eruption is ongoing and before it is safe to access on foot for direct sampling and measurement.

4.5. Further applications

Combining high-spatial resolution roughness and solar heating rate measurements represents a powerful technique for investigating volcanic deposits. As these quantities measure fundamentally different properties of a surface, classification and description of different surface types is improved by using both quantities compared to using either alone. A specific advantage to using solar heating rate to improve classification of volcanic surfaces is the sensitivity of solar heating rate to sub pixel size variations in the grain or block size of deposits. In contrast,

roughness-based determinations of grain size can only be done at the scale of the spatial resolution of the DEM, which limited the ability of previous studies using only topographic data (Mazzarini et al., 2009; Whelley et al., 2014) to describe pyroclastic deposits.

Although our study focuses on roughness and solar heating rate applied to volcanic deposits, the methods we present here can be applied to any surface type and using satellite datasets. This may be of use for analysis of depositional processes in fluvial, landslide, or glacial environments as well as terrestrial analogue applications for studies of other planetary surfaces. Investigations of surface roughness of volcanic deposits on other planets have primarily utilized orbital LiDAR or other radar datasets (e.g., Lawrence et al., 2013; Jawin et al., 2014). This study illuminates the benefit of using high spatial resolution visible datasets to create a DEM and constrain surface roughness at higher spatial resolution than orbital LiDAR. With the rapid increase of UAS utilization in the field, methods such as the one presented here pave the way to efficient mapping and classification and more data-driven applications in volcanology and earth and planetary sciences in general.

5. Conclusions

We have presented a new approach to fine-scale classification of volcanic surfaces in a basaltic flow field utilizing visual and TIR imagery collected by UAS to derive surface roughness and solar heating rate. Solar heating rate excels at identifying differences in physical properties of deposits such as grain size and density, whereas roughness is better at identifying variations in surface morphology. We used these quantities in tandem to classify and map different volcanic deposits manually and using machine learning techniques. For lava flows from the 2018 eruption of Sierra Negra volcano, we observe that the solar heating rate of the lava flow surface decreases downflow, indicative of increasing flow degassing and increasing lava density during a transition from pāhoehoe morphology near-vent to ʻaʻā further downflow.

Our simplified (three category) manual classification of the study area relied primarily on solar heating rate to differentiate between tephra, pāhoehoe lava, and ʻaʻā lava. For our refined (five category) manual classification, roughness was the main value separating pāhoehoe crust from slabby pāhoehoe and ridged ʻaʻā from blocky ʻaʻā. The manual classification broadly agreed with the location of surface types we visually identified in the field. The supervised machine learning method matches the manual classifications with an accuracy greater than 80%, showing its ability to map known deposit types. The unsupervised machine learning method was not able to match the surface types we identified well enough to be useful for mapping (accuracy ~60%), though it successfully separated tephra from the lava flow without initial ground truth information. When applied in appropriate cases, classification via machine learning can improve on the capability of manual classification.

Many advantages exist for using UAS to measure solar heating rate and roughness at high spatial resolution. The use of UAS enables data collection on short time-scales and at specific times. In contrast, to determine ATI from satellite it can be necessary to wait weeks or longer for the satellite to capture a cloud-free day-night pair of images. The high spatial resolution of our UAS data (0.2 m) also allowed us to avoid issues related to sub-pixel mixing of surface types that occur when using coarser resolution satellite data. We used the location of the classified surface morphologies to identify the pāhoehoe-to-ʻaʻā transition, main flow channel, and breakout flow lobes. This enabled us to infer conditions related to emplacement of the lava flow. Unlike roughness, solar heating rate can be used to observe variations in grain size at sub-pixel scales. Our approach can be applied in a variety of depositional environments and used for planetary analog studies to provide insight on surface process on earth and other planetary bodies.

Declaration of Competing Interest

The authors declare that they have no known competing financial interests or personal relationships that could have appeared to influence the work reported in this paper.

The authors declare the following financial interests/personal relationships which may be considered as potential competing interests.

Acknowledgments

This work was supported by NSF EAR Postdoctoral Fellowship Award #1725768 and a WHOI Independent Research and Development Grant (PI: Adam Soule). EL was supported by NSF award EAR-1654588. Field work in Ecuador was conducted in cooperation with the Instituto Geofísico, the Parque Nacional Galápagos, and the Charles Darwin Research Station. Marco Córdova of Instituto Geofísico and Meghan Jones of Woods Hole Oceanographic Institute assisted with data collection at Sierra Negra. Field work in Indonesia was conducted under a memorandum of understanding between Arizona State University (Tempe, AZ, USA) and Universitas Gadjah Mada (Yogyakarta, Indonesia). Danielle Moyer and Emily Carey of Drexel University and Aldaka Wiguna and Reza Firdaus Nasution of Universitas Gadjah Mada assisted with data collection at Sinabung Volcano. Any use of trade, firm, or product names is for descriptive purposes only and does not imply endorsement by the U.S. Government.

Appendix A. Supplementary data

Supplementary data to this article can be found online at https://doi.org/10.1016/j.rse.2021.112581.

References

Bemis, S.P., Micklethwaite, S., Turner, D., James, M.R., Akciz, S., Thiele, S.T., Bangash, H.A., 2014. Ground-based and UAV-based photogrammetry: a multi-scale, high-resolution mapping tool for structural geology and paleoseismology. J. Struct. Geol. 69, 163–178. https://doi.org/10.1016/j.jsg.2014.10.007.

Bretar, F., Arab-Sedze, M., Champion, J., Pierrot-Deseilligny, M., Heggy, E., Jacquemoud, S., 2013. An advanced photogrammetric method to measure surface roughness: application to volcanic terrains in the piton de la Fournaise, Reunion Island. Remote Sens. Environ. 135, 1–11. https://doi.org/10.1016/j.rse.2013.03.026.

Charbonnier, S.J., Gertisser, R., 2008. Field observations and surface characteristics of pristine block-and-ash flow deposits from the 2006 eruption of Merapi volcano, Java, Indonesia. J. Volcanol. Geotherm. Res. 177, 971–982. https://doi.org/10.1016/j.jvolgeores.2008.07.008.

Corradino, C., Ganci, G., Cappello, A., Bilotta, G., Hérault, A., Negro, C.D., 2019. Mapping recent lava flows at Mount Etna using multispectral Sentinel-2 images and machine learning techniques. Remote Sens. 11, 1916. https://doi.org/10.3390/rs11161916.

Crown, D.A., Ramsey, M.S., 2017. Morphological and thermophysical characteristics of lava flows southwest of Arsia Mons, Mars. J. Volcanol. Geotherm. Res. 342, 13–28. https://doi.org/10.1016/j.jvolgeores.2016.07.008.

Fergason, R.L., Christensen, P.R., Kieffer, H.H., 2006. High-resolution thermal inertia derived from the thermal emission imaging system (THEMIS): thermal model and applications. J. Geophys. Res. 111, E12004 https://doi.org/10.1029/2006JE002735.

Fink, J.H., Griffiths, R.W., 1992. A laboratory analog study of the surface morphology of lava flows extruded from point and line sources. J. Volcanol. Geotherm. Res. 54, 19–32. https://doi.org/10.1016/0377-0273(92)90112-q.

Ganci, G., Cappello, A., Bilotta, G., Herault, A., Zago, V., Negro, C.D., 2018. Mapping volcanic deposits of the 2011–2015 Etna eruptive events using satellite remote sensing. Front. Earth Sci. 6, 83. https://doi.org/10.3389/feart.2018.00083.

Geist, D.J., Harpp, K.S., Naumann, T.R., Poland, M., Chadwick, W.W., Hall, M., Rader, E., 2007. The 2005 eruption of Sierra Negra volcano, Galápagos, Ecuador. Bull. Volcanol. 70, 655–673. https://doi.org/10.1007/s00445-007-0160-3.

Griffiths, R.W., 2000. The dynamics of lava flows. Annu. Rev. Fluid Mech. 32, 477–518. https://doi.org/10.1146/annurev.fluid.32.1.477.

Grohmann, C.H., Smith, M.J., Riccomini, C., 2011. Multiscale analysis of topographic surface roughness in the Midland Valley, Scotland. IEEE Trans. Geosci. Remote Sens. 49, 1200–1213. https://doi.org/10.1109/TGRS.2010.2053546.

James, M.R., Robson, S., 2012. Straightforward reconstruction of 3D surfaces and topography with a camera: accuracy and geoscience application. J. Geophys. Res. 117, F03017 https://doi.org/10.1029/2011JF002289.

James, M.R., Chandler, J.H., Eltner, A., Fraser, C., Miller, P.E., Mills, J.P., Noble, T., Robson, S., Lane, S.N., 2019. Guidelines on the use of structure-from-motion

photogrammetry in geomorphic research. Earth Surf. Process. Landf. https://doi.org/10.1002/esp.4637.

James M R, Carr B B, D'Arcy F, Diefenbach A K, Dietterich H R, Fornaciai A, Lev E, Liu E J, Pieri D C, Rodgers M, Smets B, Terada A, von Aulock F W, Walter T R, Wood K T, Zorn E U (2020a). Volcanological applications of unoccupied aircraft systems (UAS): developments, strategies, and future challenges. Volcanica 3:67–114. Doi:10.30909/vol.03.01.67114.

James, M.R., Antoniazza, G., Robson, S., Lane, S.N., 2020b. Mitigating systematic error in topographic models for geomorphic change detection: accuracy, precision and considerations beyond off-nadir imagery. Earth Surf. Process. Landf. 45, 2251–2271. https://doi.org/10.1002/esp.4878.

Jawin, E.R., Kiefer, W.S., Fassett, C.I., Bussey, D.B.J., Cahill, J.T.S., Dyar, M.D., Lawrence, S.J., Spudis, P.D., 2014. The relationship between radar scattering and surface roughness of lunar volcanic features. J. Geophys. Res.: Planets 119, 2331–2348. https://doi.org/10.1002/2014je004668.

Kereszturi, G., Schaefer, L.N., Schleiffarth, W.K., Procter, J., Pullanagari, R.R., Mead, S., Kennedy, B., 2018. Integrating airborne hyperspectral imagery and LiDAR for volcano mapping and monitoring through image classification. Int. J. Appl. Earth Obs. Geoinf. 73, 323–339. https://doi.org/10.1016/j.jag.2018.07.006.

Lawrence, S.J., Stopar, J.D., Hawke, B.R., Greenhagen, B.T., Cahill, J.T.S., Bandfield, J. L., Jolliff, B.L., Denevi, B.W., Robinson, M.S., Glotch, T.D., Bussey, D.B.J., Spudis, P. D., Giguere, T.A., Garry, W.B., 2013. LRO observations of morphology and surface roughness of volcanic cones and lobate lava flows in the Marius Hills. J. Geophys. Res.: Planets 118, 615–634. https://doi.org/10.1002/jgre.20060.

Li, L., Solana, C., Canters, F., Kervyn, M., 2017. Testing random forest classification for identifying lava flows and mapping age groups on a single Landsat 8 image. J. Volcanol. Geotherm. Res. 345, 109–124. https://doi.org/10.1016/j.jvolgeores.2017.07.014.

Lipman, P.W., Banks, N.G., 1987. Aa flow dynamics, Mauna Loa 1984. U.S. Geological Survey Professional Paper 1350: Volcanism in Hawaii, pp. 1527–1567.

Mazzarini, F., Favalli, M., Isola, I., Neri, M., Pareschi, M.T., 2009. Surface roughness of pyroclastic deposits at Mt. Etna by 3D laser scanning. Ann. Geophys. 51, 813–822. https://doi.org/10.4401/ag-4461.

Morris, A.R., Anderson, F.S., Mouginis-Mark, P.J., Haldemann, A.F.C., Brooks, B.A., Foster, J., 2008. Roughness of Hawaiian volcanic terrains. J. Geophys. Res. 113, E12007 https://doi.org/10.1029/2008je003079.

Nakada, S., Zaennudin, A., Yoshimoto, M., Maeno, F., Suzuki, Y., Hokanishi, N., Sasaki, H., Iguchi, M., Ohkura, T., Gunawan, H., Triastuty, H., 2019. Growth process of the lava dome/flow complex at Sinabung volcano during 2013-2016. J. Volcanol. Geotherm. Res. 382, 120–136. https://doi.org/10.1016/j.jvolgeores.2017.06.012.

Pallister, J., Wessels, R.L., Griswold, J., McCausland, W., Kartadinata, N., Gunawan, H., Budianto, A., Primulyana, S., 2019. Monitoring, forecasting collapse events, and mapping pyroclastic deposits at Sinabung volcano with satellite imagery. J. Volcanol. Geotherm. Res. 382, 149–163. https://doi.org/10.1016/j.jvolgeores.2018.05.012.

Pedregosa, F., Varoquaux, G., Gramfort, A., Michel, V., Thirion, B., Grisel, O., Blondel, M., Prettenhofer, P., Weiss, R., Dubourg, V., Vanderplas, J., Passos, A., Cournapeau, D., Brucher, M., Perrot, M., Duchesnay, E., 2011. Scikit-learn: machine learning in Python. J. Mach. Learn. Res. 12, 2825–2830.

Price, J.C., 1977. Thermal inertia mapping: a new view of the earth. J. Geophys. Res. 82, 2582–2590. https://doi.org/10.1029/jc082i018p02582.

Price, M.A., Ramsey, M.S., Crown, D.A., 2016. Satellite-based Thermophysical analysis of Volcaniclastic deposits: a terrestrial analog for mantled lava flows on Mars. Remote Sens. 8, 152. https://doi.org/10.3390/rs8020152.

Ramsey, M.S., Fink, J.H., 1999. Estimating silicic lava vesicularity with thermal remote sensing: a new technique for volcanic mapping and monitoring. Bull. Volcanol. 61, 32–39. https://doi.org/10.1007/s004450050260.

Ramsey, M.S., Harris, A.J.L., Crown, D.A., 2016. What can thermal infrared remote sensing of terrestrial volcanoes tell us about processes past and present on Mars? J. Volcanol. Geotherm. Res. 311, 198–216. https://doi.org/10.1016/j.jvolgeores.2016.01.012.

Richardson, P., Karlstrom, L., 2019. The multi-scale influence of topography on lava flow morphology. Bull. Volcanol. 81, 21. https://doi.org/10.1007/s00445-019-1278-9.

Rumpf, M.E., Lev, E., Wysocki, R., 2018. The influence of topographic roughness on lava flow emplacement. Bull. Volcanol. 80, 63. https://doi.org/10.1007/s00445-018-1238-9.

Scheidt, S., Ramsey, M.S., Lancaster, N., 2010. Determining soil moisture and sediment availability at White Sands dune field, New Mexico, from apparent thermal inertia data. J. Geophys. Res. 115, F02019 https://doi.org/10.1029/2009JF001378.

Shepard, M.K., Campbell, B.A., Bulmer, M.H., Farr, T.G., Gaddis, L.R., Plaut, J.J., 2001. The roughness of natural terrain: a planetary and remote sensing perspective. J. Geophys. Res.: Planets 106, 32777–32795. https://doi.org/10.1029/2000je001429.

Simurda, C., Ramsey, M., Scheidt, S., 2020. Assessing lava flow subpixel surface roughness and particle size distribution for improved thermal inertia interpretations. Remote Sens. 12, 2914. https://doi.org/10.3390/rs12182914.

Solikhin, A., Pinel, V., Vandemeulebrouck, J., Thouret, J.-C., Hendrasto, M., 2015. Mapping the 2010 Merapi pyroclastic deposits using dual-polarization synthetic aperture radar (SAR) data. Remote Sens. Environ. 158, 180–192. https://doi.org/10.1016/j.rse.2014.11.002.

Soule, S.A., Karlstrom, L., Lev, E., Carr, B.B., Jones, M., Vallejo Vargas, S., Córdova Aguilar, M.D., Mikesell, D., Paustian, J., Kubo, A., Michel, A.P., Pardis, W., 2019. Sierra Negra Eruption, Galápagos, Ecuador, Abstract V23C-02 presented at 2019 Fall Meeting. AGU, San Francisco, CA, 9-13 Dec.

Vasconez F, Ramón P, Hernandez S, Hidalgo S, Bernard B, Ruiz M, Alvarado A, LaFemina P, Ruiz G (2018). The different characteristics of the recent eruptions of Fernandina and sierra Negra volcanoes (Galápagos, Ecuador). Volcanica 1:127–133. Doi:10.30909/vol.01.02.127133.

Waske, B., Benediktsson, J.A., Arnason, K., Sveinsson, J.R., 2009. Mapping of hyperspectral AVIRIS data using machine-learning algorithms. Can. J. Remote. Sens. 35, S106–S116. https://doi.org/10.5589/m09-018.

Whelley, P.L., Glaze, L.S., Calder, E.S., Harding, D.J., 2014. LiDAR-derived surface roughness texture mapping: application to mount St. Helens Pumice plain deposit analysis. IEEE Trans. Geosci. Remote Sens. 52, 426–438. https://doi.org/10.1109/TGRS.2013.2241443.

Whelley, P.L., Garry, W.B., Hamilton, C.W., Bleacher, J.E., 2017. LiDAR-derived surface roughness signatures of basaltic lava types at the Muliwai a Pele Lava Channel, Mauna Ulu, Hawai'i. Bull. Volcanol. 79, 75. https://doi.org/10.1007/s00445-017-1161-5.

Wooster, M.J., Kaneko, T., Nakada, S., Shimizu, H., 2000. Discrimination of lava dome activity styles using satellite-derived thermal structures. J. Volcanol. Geotherm. Res. 102, 97–118. https://doi.org/10.1016/S0377-0273(00)00183-9.